Chapter 4

The 21st century climate as simulated by LMD5-CLIO2

The aim of this thesis is to investigate the 21st century climate. Therefore LMD5-CLIO2-GISM has been developed (chapter 2). Its AOGCM component (LMD5-CLIO2) has been validated in chapter 3. This tool is now used to provide climate projections for the 21st century. More precisely, this chapter is divided in two parts: one devoted to the LMD5-CLIO2 response to the greenhouse-gas and sulphate-aerosol modifications, and one dealing with the impact of the Greenland ice-sheet freshwater flux.

In the first part, the SRESb2 simulation, whose design is described in chapter 2, is analyzed. Both the effects of the enhanced greenhouse-gas concentration and of the sulphate aerosols are included in this experiment. Therefore no attempt is made to distinguish between them. To estimate the reliability of the LMD5-CLIO2 results, they are compared to those obtained with other AOGCMs. Furthermore, the time evolution is briefly described but we focus on the SRESb2 forecast for the end of the 21st century when the climatic response is highest.

In the second part, the SRESb2G and SRESb2 experiments are compared to investigate the influence of the increase of the Greenland ice-sheet runoff. A collapse of the NADW formation is forecasted at the end of the SRESb2 run. This event is induced by the freshening of the surface water due to the enhanced Greenland ice-sheet freshwater flux. In a last section, the climatic impacts of this abrupt weakening of the North Atlantic branch of the thermohaline circulation are described.

4.1 Climate change induced by greenhouse gases and sulphate aerosols

The increase in atmospheric greenhouse-gas concentration perturbs the climate system. The energy cycle is modified with more infrared radiation trapped inside the system, thus increasing its temperature. The direct cooling effect of the sulphate aerosols is also included in the model. Both of them combine to change the thermal state of the climate system (section 4.1.1). LMD5-CLIO2 is able to forecast the geographical and vertical distribution of the warming in the atmosphere and in the ocean. The time evolution of the temperature

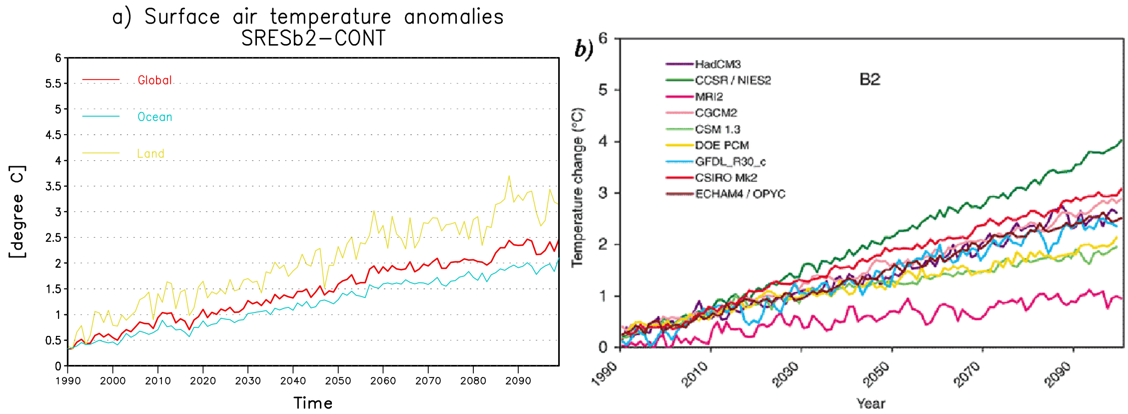

Figure 4.1: Globally averaged surface air temperature (°C). Panel a displays the results of the SRESb2 simulation compared to the CONT experiment. The red curve takes into account all model grid points. The continental temperature evolution is in yellow, and the ocean (or sea-ice) grid points are used to compute the cyan curve. Panel b from *Cubasch et al.* [2001] shows the time evolution of the globally averaged surface air temperature change relative to the years (1961 to 1990) simulated by various other AOGCMs using the SRES B2 scenario.

change is also analyzed. These modifications of the temperature field alter the hydrological cycle as the saturation level depends on temperature. Changes in the hydrological cycle are described in section 4.1.2. The humidity in the atmosphere adjusts to the new thermal conditions involving changes to the water vapour and cloudiness. The atmospheric water content is related to evaporation and precipitation. Through these, the oceanic salinity may also be altered. Finally, modifications of the temperature and salinity fields in the ocean change the density gradient, implying perturbation of the oceanic circulation. In the atmosphere, changes of temperature gradients and convection influence the atmospheric general circulation. Modifications of the dynamic fields are analyzed in section 4.1.3.

Furthermore, depending on the greenhouse-gas concentration scenario, the time rates of the modifications strongly differ. The predictions discussed hereafter are related to the SRES B2 scenario published by the IPCC[1] (*Nakićenovic et al.* [2000]). All the results show in this section come from the SRESb2 simulation whose design is described in chapter 2. We should therefore keep in mind that the dates cited are indicative.

4.1.1 Thermal response

The best known impact of climate change is the global warming. This temperature increase is not uniform. It is distributed throughout the atmosphere and the ocean.

4.1.1.1 Atmospheric temperature changes

As expected, the ***surface air temperature*** rises progressively under the influence of greenhouse gases and sulphate aerosols. The LMD5-CLIO2 response is in the middle range

[1]Intergovernmental Panel on Climate Change

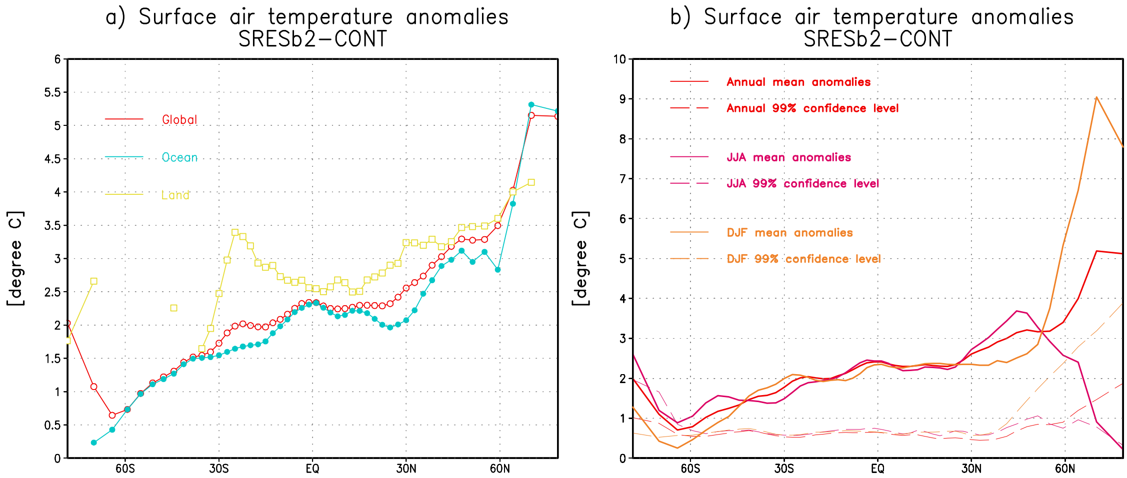

Figure 4.2: Zonal mean surface air temperature (°C) as simulated by the SRESb2 simulation compared to the CONT experiment (averaged over the last 5 years 2095-2099). The left panel (a) shows annual means. The red curve takes into account all model grid points. The continental temperature evolution is in yellow, and the ocean (or sea-ice) grid points are used to compute the cyan curve. On panel b, the solid lines are the anomalies forecasted by LMD5-CLIO2 at the end of the SRESb2 simulation in annual mean (red curve), during boreal summer (JJA, magenta curve), and during Southern Hemisphere summer (DJF, orange curve). The dashed lines are the 99% confidence level computed as 2.33 times the standard deviation from the CONT simulation.

of those predicted by other coupled models (figure 4.1a). The surface warming reaches 2.4°C in 2100 compared to the CONT simulation (1970), while the range suggested in *Cubasch et al.* [2001] (for a similar period) is 0.9°C to 3.4°C (figure 4.1b). For the middle of the 21st century, the globally averaged surface air temperature increase is estimated by other models to be between 0.5°C and 1.7°C. Our estimate is about 1.4°C. In fact, the warming is more or less linear in all simulations using this scenario (figure 4.1a). The behaviour of continental grid points and oceanic grid points differ: the first ones undergo a greater warming than the second ones. The only exception are the points located at high latitudes, where the ocean is covered by sea ice (figure 4.2a). The interannual variability is also more pronounced over land, which is not surprising as the oceanic time scales are longer than the atmospheric ones.

Another interesting feature is the ***meridional asymmetry*** (figure 4.2). The temperature response in the Northern Hemisphere is more pronounced than in the Southern Hemisphere. This asymmetry is obvious in the oceanic response. At mid-latitudes, the Southern Ocean undergoes a very small warming at most longitudes compared to the same latitudes in the Northern Hemisphere[2]. Deep convection is simulated at these latitudes (see chapter 3). It distributes the "exceeding" heat, trapped by the greenhouse gases, over a deeper oceanic layer than at other latitudes (see section 4.1.1.2). Consequently, the

[2]Two major exceptions exist: a strong temperature increase is located in the Ross Sea, and a cooling is forecasted in the Weddell Sea.

water-temperature anomalies near the surface are small. The turbulent heat fluxes imply a strong coupling between the sea-surface temperature and the surface air temperature. So, a weak warming of the surface air is simulated at these latitudes. At higher latitudes, the Arctic Ocean undergoes a strong reduction of the sea-ice pack (see section 4.1.4). Consequently, the temperature increase is enhanced by the albedo/temperature feedback (see chapter 1, and section 4.1.4). On the contrary, the southern high latitudes are covered by the Antarctic continent, where this feedback is not active: the continental ice-sheet is so thick that a partial melting would not significantly change its albedo. This effect however is not taken into account in LMD5-CLIO2 over ice sheets. The meridional asymmetry is also partially due to the distribution of continents over the Earth. As the largest fraction of the continents is located in the Northern Hemisphere and as the continental temperature response is greater than the oceanic one, the temperature rise is stronger in the Northern Hemisphere. This feature is not specific to LMD5-CLIO2, most models simulate this asymmetry (*Cubasch et al.* [2001]). This point has been discussed for example in *Houghton et al.* [1996]. One of the rare models which do not forecast this asymmetry is CGCM2 of the Canadian Centre for Climate Modelling and Analysis (*Flato and Boer* [2001]).

Seasonally, the asymmetry is always present between 60°S and 45°N. Northwards and especially over the Arctic Ocean, the LMD5-CLIO2 response is very different in summer (JJA) and in winter (DJF). The summer surface temperature increase is very small while the winter surface warming reaches 9°C. This behaviour is due to sea ice as explained later (see section 4.1.4). The seasonal cycle of the SRESb2 simulation response is small in the intertropical regions. At mid latitudes, the summer warming is bigger than the winter warming (the opposite of what happens at high latitudes).

To estimate the ***significance*** of this warming (figure 4.2b), the standard deviation of the zonally averaged surface air temperature has been computed from the CONT experiment (years 21 to 150). The warming is significant if it is larger than 2.33 times this standard deviation (99% confidence level). In annual mean, the surface air temperature change is significant at all latitudes. Seasonally, the increase in zonally averaged surface air temperature is not always significant over the Southern Ocean and over the Arctic Ocean in summer as the temperature increase is very small.

The only base to evaluate the realism of the climate change forecasted by LMD5-CLIO2 are results from other models. It is therefore interesting to compare the ***horizontal distribution*** of the surface air warming in the SRESb2 simulation with that obtained with other coupled models. Nine coupled models had run under the SRES B2 scenario prior to the writing of the IPCC Third Assessment Report (*Cubasch et al.* [2001]). Their results have been collected and summarized in that report. Each model produces a somewhat different projection. Computing the multi-model ensemble mean averages to zero the variability. It could also been expected that the systematic errors from all the models also tend to average out. This assumes that the systematic errors are different in various unrelated models. Consequently, this multi-model approach should produce a better estimate of the forced climate change of the real system than the result from any particular model. The ensemble standard deviation and the range are used as available indications of uncertainty in model results. It is accepted in this report that the ensemble mean divided by its standard deviation provides a measure of the consistency of the climate change patterns. Values greater than 1.0 are a conservative estimate of areas of consistent model response. Figure 4.3b

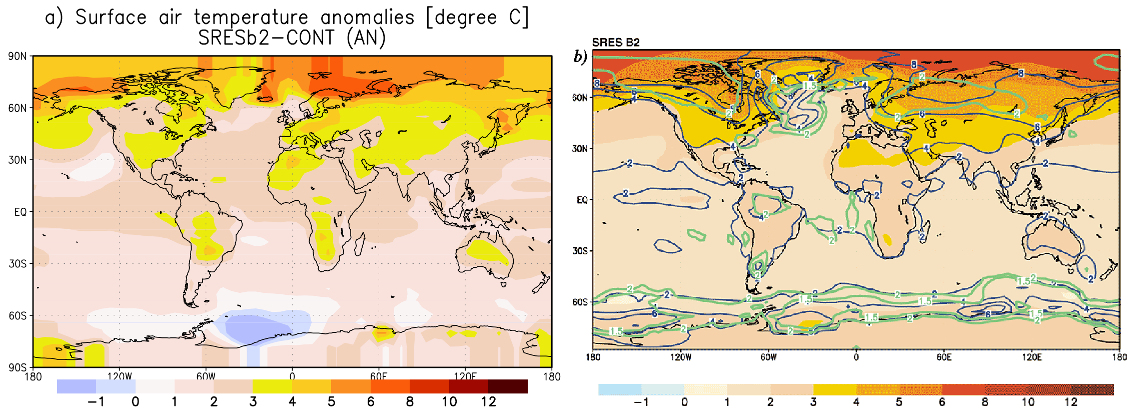

Figure 4.3: Panel a displays the annual mean surface air temperature anomalies between the SRESb2 experiment and the CONT simulation (°C). The SRESb2 and CONT simulation results have been averaged over the last 5 years (2095-2099) prior to computing their difference. Panel b comes from *Cubasch et al.* [2001] and provides the multi-model ensemble annual mean change of the surface air temperature (color shading), its range (thin blue isolines) (°C), and the multi-model mean change divided by the multi-model standard deviation (solid green isolines, absolute values).

comes from *Cubasch et al.* [2001]. It contains this kind of information. The multi-model ensemble annual change is color shaded, its range is shown by the blue isolines, and the multi-model mean change divided by the multi-model standard deviation is displayed with the green isolines. Compared to our results (figure 4.3a), the overall patterns are similar. The stronger warming is located over the Arctic Ocean, the minimum is simulated over the Southern Ocean, the surface air temperature increase is stronger over continents than over the oceans. Beyond this first impression, local discrepancies appear. A cooling is simulated by LMD5-CLIO2 in the Weddell sea, while the multi-model ensemble mean exhibits a warming in the same region. Nevertheless, the multi-model range is large over there so, cooling is probably simulated by other models. The surface air warming over the Southern Hemisphere continents is stronger in LMD5-CLIO2 (reaching 5°C) than in the multi-model ensemble mean. Again, the multi-model warming reaches 3°C and its range is more than 2°C. So, although our results are at the upper limit, they remain "realistic". An asymmetry between western and eastern Sahara is visible in the multi-model ensemble mean, but it is more pronounced in the SRESb2 experiment results. The surface air temperature warming forecasted by LMD5-CLIO2 is more intense than the multi-model ensemble mean. On the contrary, the temperature increase in the SRESb2 experiment is smaller over Russia and over the Arctic Ocean. The IPCC Third Assessment Report (*Cubasch et al.* [2001]) mentions that most models show a minimum of warming somewhere over the North Atlantic Ocean (but the location is quite variable). It is also the case in our simulation.

The zonal mean ***vertical pattern*** of temperature change is displayed in figure 4.4. The annual mean (figure 4.4a) indicates the main characteristics of the global warming distribution according to latitude and altitude. We will first focus on the atmosphere.

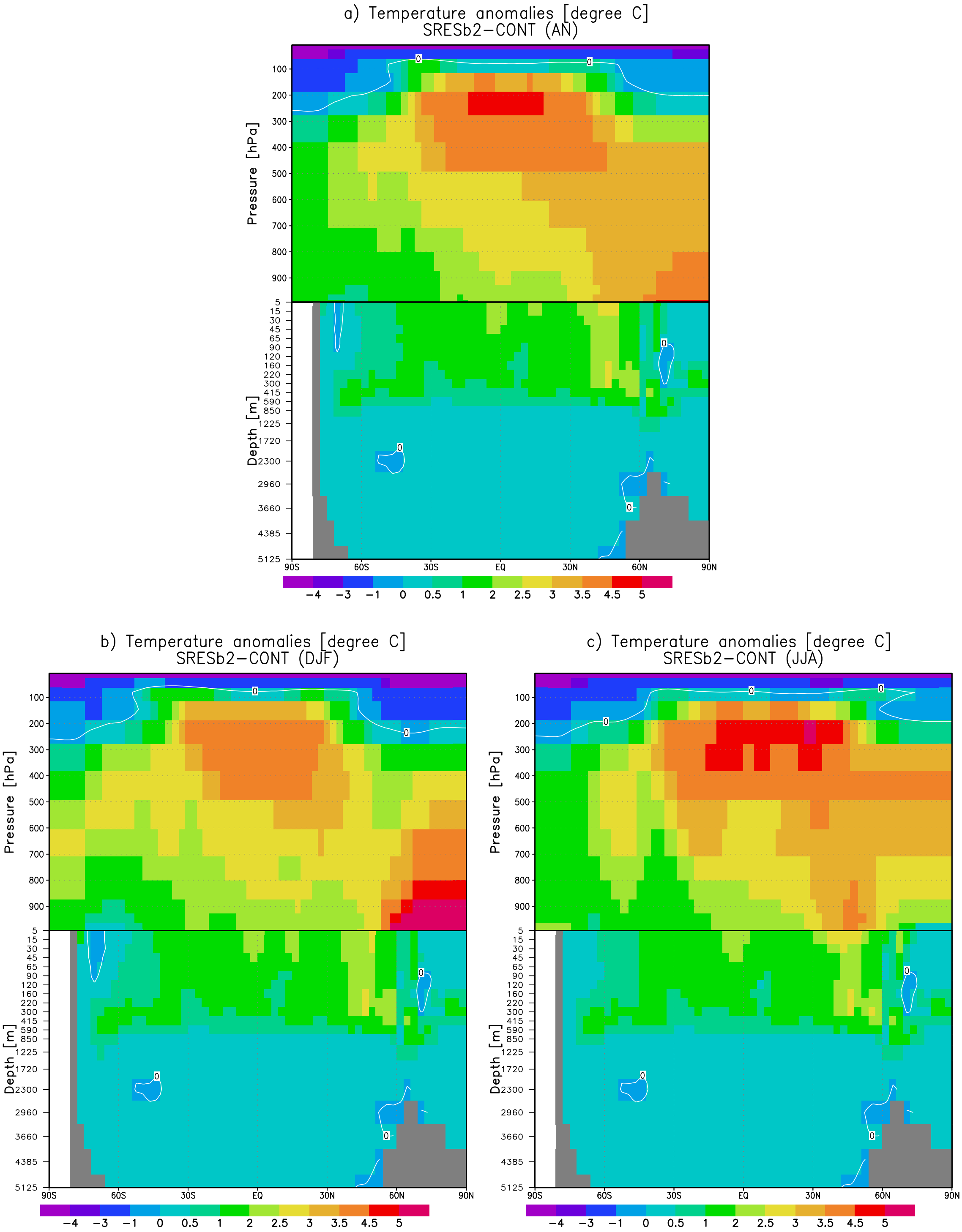

Figure 4.4: Zonal mean vertical patterns of temperature change (°C) in the SRESb2 simulation compared to the CONT integration. Panel a shows the annual mean, while the December-January-February (DJF) and June-July-August (JJA) means are displayed on panels b and c, respectively. The SRESb2 and CONT results have been averaged over the last 5 years (2095-2099).

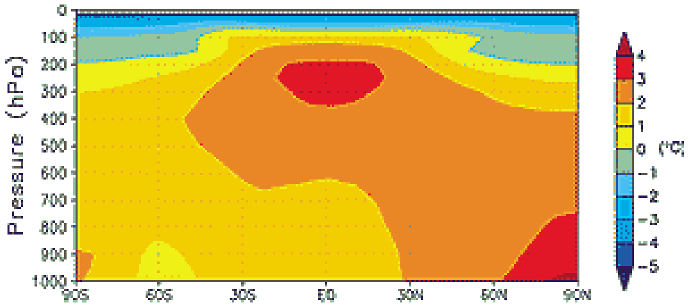

Figure 4.5: Multi-model annual mean zonal temperature change for the CMIP2 simulations from *Cubasch et al.* [2001].

The maximum annual mean atmospheric warming is located near 200 hPa in the tropical region. Convective activity is slightly higher in a warmer climate, and stronger vertical motions bring the tropopause higher. The two other panels (figure 4.4b, c) show the seasonal cycle. They indicate that the maximum warming migrates slightly towards the summer hemisphere with the upward branch of the Hadley cells. Furthermore, as the most predominant cell is in the winter hemisphere, the warming spreads down near 30°N in December-January-February (DJF), or near 30°S in June-July-August (JJA). The summer hemisphere cell also propagates the warming towards the surface especially in JJA near 35°N. Looking at the annual mean, a second maximum is forecasted in the lower troposphere over the Arctic region. It is very strong in DJF (winter) whereas nearly no temperature change is simulated in JJA. The surface air temperature is strongly coupled to the surface temperature by turbulent fluxes. At these high latitudes, the oceanic surface is partially covered by sea ice. In summer, sea ice is melting in the CONT simulation as in the SRESb2 experiment. Consequently, the summer surface-temperature anomalies are small.

Moreover, the patterns obtained with LMD5-CLIO2 are very similar to those of other models. The composite of the zonal temperature changes obtained by the models participating to CMIP2[3] (*Meehl et al.* [2000]) is shown in figure 4.5. While comparing these figures, we should keep in mind that the scenario differs and that the period in the future is also different.

4.1.1.2 Oceanic temperature changes

The infrared radiation trapped by greenhouse gases warms the atmosphere but also the ocean. Unlike the atmosphere, the ocean is warmed at its top. The oceanic warming (figure 4.4) is mainly restrained to the ***upper*** 300 m where the vertical mixing is strong enough. Its intensity follows mainly the pattern of the surface air temperature anomalies. A major exception is the Northern Hemisphere high latitudes: whereas the Arctic region undergoes a very intense temperature increase in the low troposphere, the anomalies in the ocean are negligible. In fact, sea ice insulates the ocean from the atmospheric influence;

[3]CMIP2 is the second phase of the Coupled Model Intercomparison Project, which deals with 1% CO_2 increase simulations.

moreover, no significant modification of the ***sea-surface temperature*** may occur prior to an important melting of sea ice. In other words, the exceeding heat available at the surface would first leads to phase transition before inducing any temperature change. Furthermore, the seasonal variability of the oceanic temperature simulated by LMD5-CLIO2 is much smaller than in the atmosphere: figure 4.4b and figure 4.4c are very similar for the ocean.

Looking at the anomalies in each basin (figure 4.6), another feature becomes apparent. In the Southern Ocean, the warming maximum is not located at the surface but ***deeper***. In the Atlantic sector, the surface cooling associated with the expansion of sea ice in the Weddell sea is obvious in the upper 160 m. Below, positive temperature anomalies are simulated. This warming exceeds 1°C down to about 2500 m. In the Pacific sector, no cooling is simulated near the surface but the maximum temperature rise is forecasted near 400 m. The warming obviously goes down to the bottom of the water column. This indicates that deep convection brings additional heat from the surface (due to the increase in greenhouse-gas concentrations) down to the bottom of the ocean.

In another respect, the response of the oceanic temperature above 220 m is almost linear ***in time***, similarly to the surface temperature. Below, the temperature increase is slower at the beginning of the simulation. By the end of the simulation, the warming rate nonetheless is similar at any depth in the upper 415 m. Below, the temperature response is not linear: the warming rate progressively increases. Furthermore, the deeper you go, the smaller is the warming rate. These features are expected: the deep-ocean water masses are mainly renewed by the thermohaline circulation which is much slower than the upper wind-driven circulation. The additional heat available at the surface therefore takes more time to reach greater depth.

4.1.2 Hydrological response

The atmosphere contains water vapour and liquid (or ice) water. The atmospheric warming induced by the increase in greenhouse-gas concentrations, in spite of the cooling effect of sulphate aerosols, raises the saturation vapour pressure.

4.1.2.1 Atmospheric humidity changes

As warmer air can hold more humidity before reaching saturation, it is expected that the SRESb2 experiment forecasts a wetter atmosphere than the CONT simulation. The specific humidity is indeed increased throughout the troposphere.

Two hypotheses are plausible: either the specific humidity increase results from the warming and the relative humidity remains constant, or the relative humidity is modified indicating deeper changes in the hydrological cycle. A first fact seems to attest the first assumption: looking at specific humidity, both the CONT and SRESb2 experiments share the same vertical distribution with a stronger amplitude in the SRESb2 experiment. More precisely, the vertical distribution of the absolute anomalies is very close to the initial pattern of the specific humidity (figure 4.7a), i.e., the water-vapour content rises more in regions of already high humidity. The hydrological cycle thus seems amplified and the atmosphere contains more humidity. The relative humidity anomalies confirm this hypothesis. The differences between this variable and its values in the CONT simulation are small: its relative anomalies remains below 10 % in the troposphere. The only exceptions

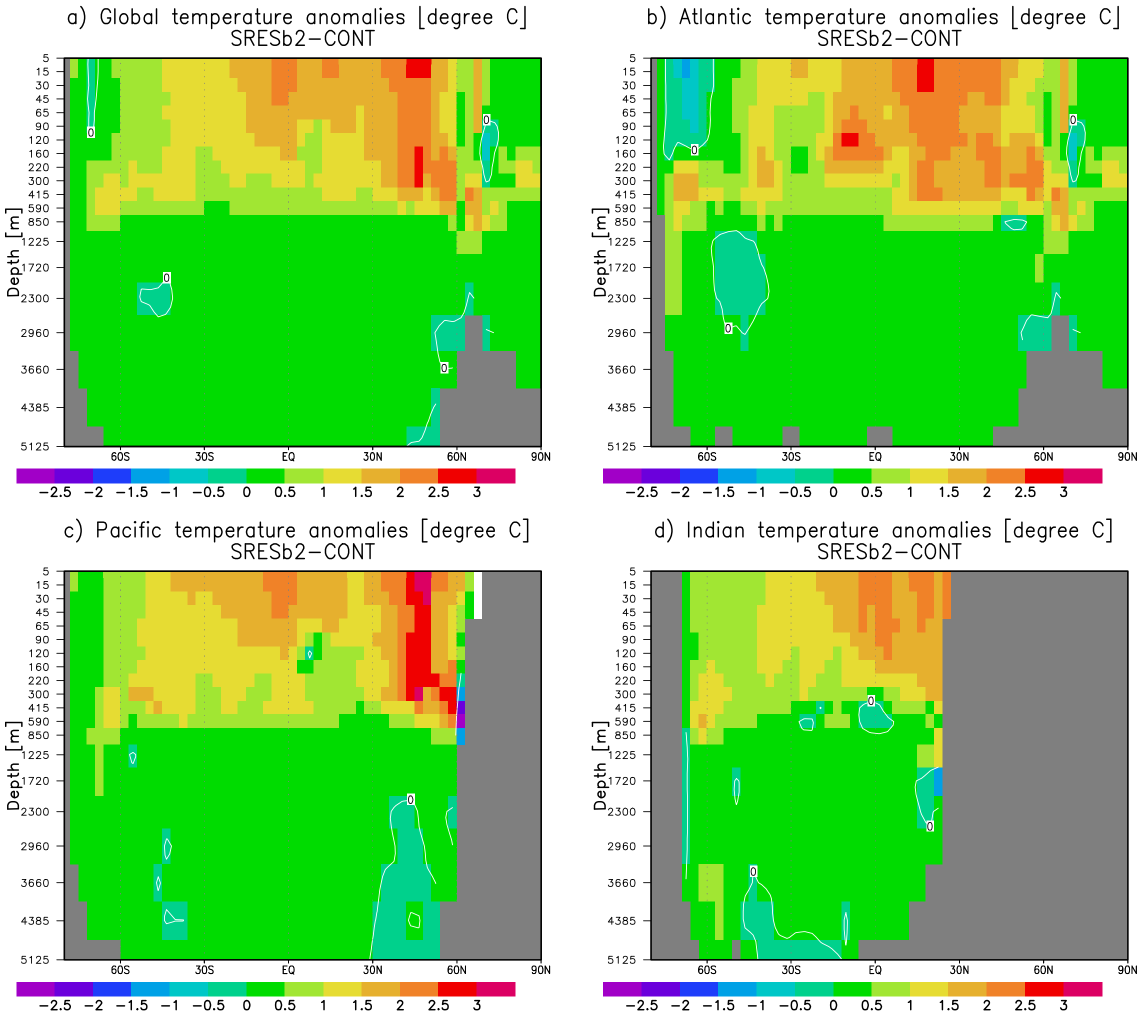

Figure 4.6: Oceanic temperature anomalies (°C) in the World Ocean zonal mean (panel a), in the Atlantic basin (panel b), and in the Pacific and Indian basins (panels c and d). The SRESb2 and CONT simulation results have been averaged over the last 5 years (2095-2099) prior to computing their difference.

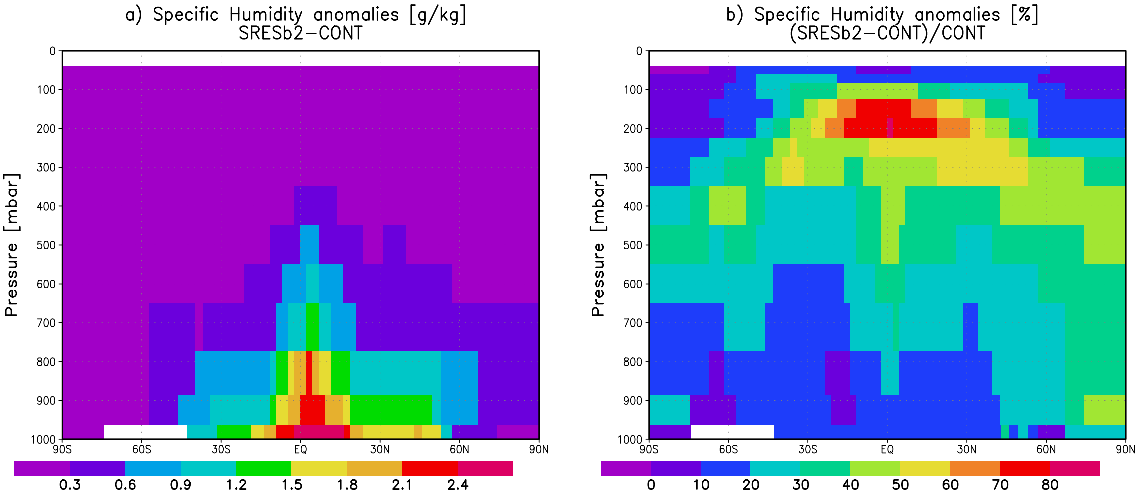

Figure 4.7: Annual mean, zonally averaged specific humidity anomalies between the CONT simulation and the SRESb2 experiment. The differences are shown in panel a (g_{water}/kg_{air}), and the relative anomalies (the differences divided by the CONT simulation values) are plotted in panel b (%). The SRESb2 and CONT simulation results have been averaged over the last 5 years (2095-2099) prior to computing their difference.

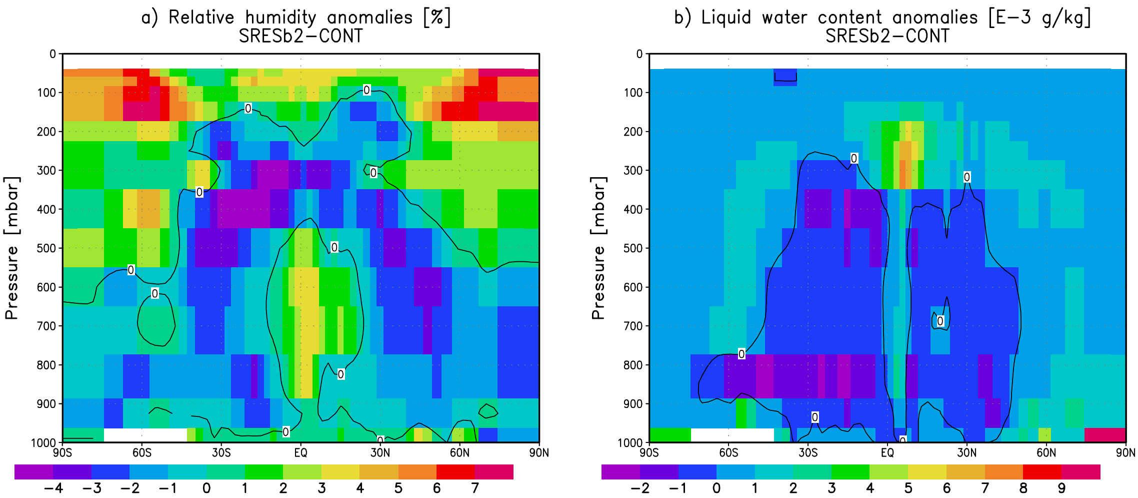

Figure 4.8: The annual mean, zonally averaged relative humidity anomalies (%) between the CONT simulation and the SRESb2 experiment are shown in panel a. Panel b displays the liquid water content anomalies (g_{water}/kg_{air}). The SRESb2 and CONT simulation results have been averaged over the last 5 years (2095-2099) prior to computing their difference.

are located in the upward branches of the Hadley cells either in June-July-August or in December-January-February. This first indications suggest that the situation is not as simple as initially thought. The hydrological processes are more deeply altered in the tropics; this is not only a direct impact of the temperature increase. Coming back to the specific humidity and focusing on the tropics, we note that the relative anomalies (figure 4.7b) are stronger in the high tropical troposphere (between 200 mbar and 100 mbar) where the specific humidity increases by more than 60 %. Furthermore, the relative humidity (figure 4.8a) increases in the ascending parts of the Hadley cells up to 400 mbar. On the contrary, it is reduced in the high troposphere at the top of these upward branches and consequently in the downward branches in both hemispheres. A possible explanation of these features is as follow. More water vapour converges at the base of the upward branches. This humidity is lifted up by the upward motion, increasing specific humidity and relative humidity. At its top, where condensation occurs, this phase transition releases heat into the atmosphere, thus increasing the air temperature. It is the location of the maximum warming (see section 4.1.1.1). Consequently, the saturation vapour pressure increases. In spite of the increase of the humidity inflow by the upward motion, the saturation vapour pressure increases quicker leading to a reduction of the relative humidity around 300 mbar and in the descending parts of the Hadley cells. The intensification of the upward transport of humidity by the Hadley cells in the ITCZ is corroborated by liquid water content and cloud fields. More liquid water (figure 4.8b) is present throughout the troposphere in the upward branches of the Hadley cells and especially between 300 mbar and 200 mbar, where the majority of the condensation occurs. The cloud fraction is also enhanced in this convective region up to 300 mbar. Above, the reduction in relative humidity is associated to the reduction of the cloudiness. This decrease propagates into the downward branches of the Hadley cells.

4.1.2.2 Surface freshwater flux modifications

As expected above from the humidity fields, the hydrological cycle is amplified in the SRESb2 simulation compared to the CONT simulation. This prediction for the 21st century is commonly admitted throughout the climatological scientific community as expressed in *Cubasch et al.* [2001]. LMD5-CLIO2 forecasts a more or less ***linear increase of the precipitation***. The precipitation relative anomalies go up to 3.3 % at the end of the 21st century; this value is in the middle range of the values forecasted by other models (figure 4.9). The evaporation follows the same evolution indicating that the atmosphere reacts with very short time-scales. An increase in evaporation brings more water into the atmosphere, and precipitation also increases. No delay is visible between the time evolution of annual mean precipitation and evaporation averaged over the globe.

The intensification of evaporation and precipitation is obvious over the ***oceans***. A positive trend of precipitation (and evaporation) is also simulated by LMD5-CLIO2 over the ***continents*** until 2050. After that, high variability is forecasted with no significant trend. Continents sometimes receive less rainfall, and evaporation is then also reduced. In fact, there is a positive feedback linking precipitation and evaporation. In many continental regions, most of the water precipitating comes from evaporation in the vicinity. So, if evaporation decreases, less water is available for precipitation and less precipitation occurs.

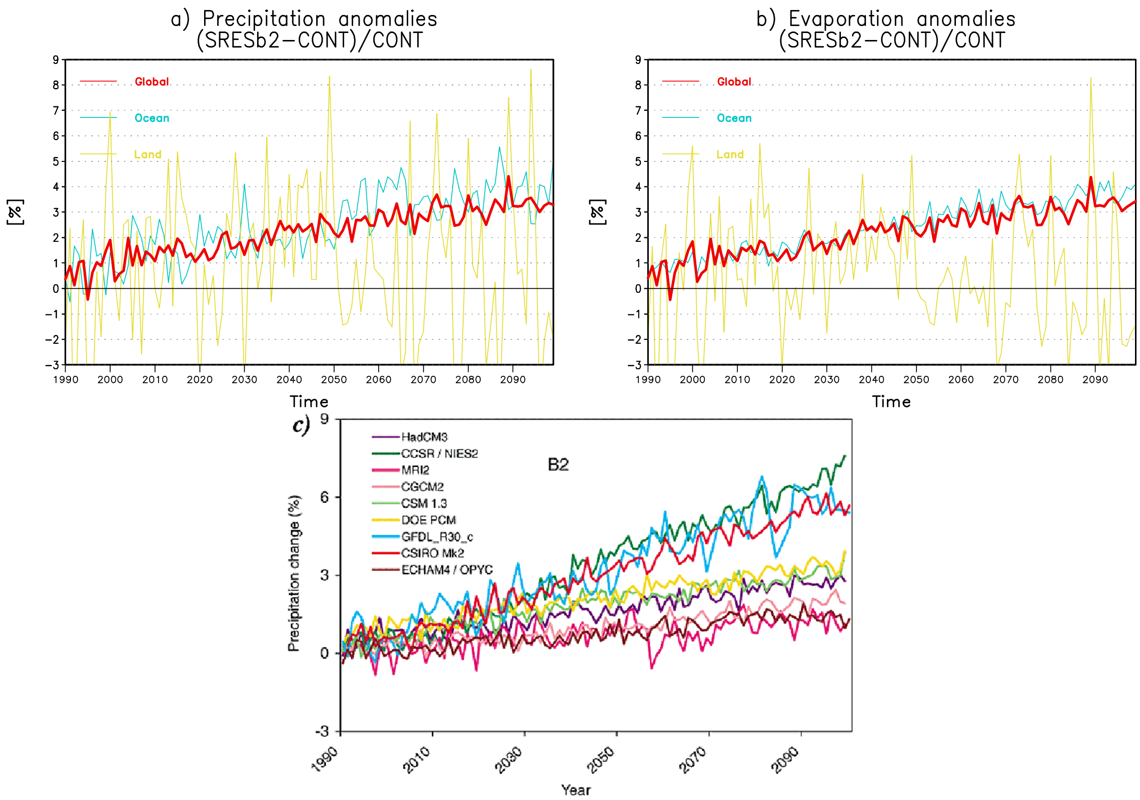

Figure 4.9: Globally averaged precipitation changes (%). Panel a displays the results of the SRESb2 simulation compared to the CONT experiment. The red curve takes into account all model grid points. The continental evolution is in yellow, and the ocean (or sea-ice) grid points are used to compute the cyan curve. Panel b is analogous to panel a but for evaporation instead of precipitation. Panel c from *Cubasch et al.* [2001] shows the globally averaged precipitation changes simulated by various other AOGCMs.

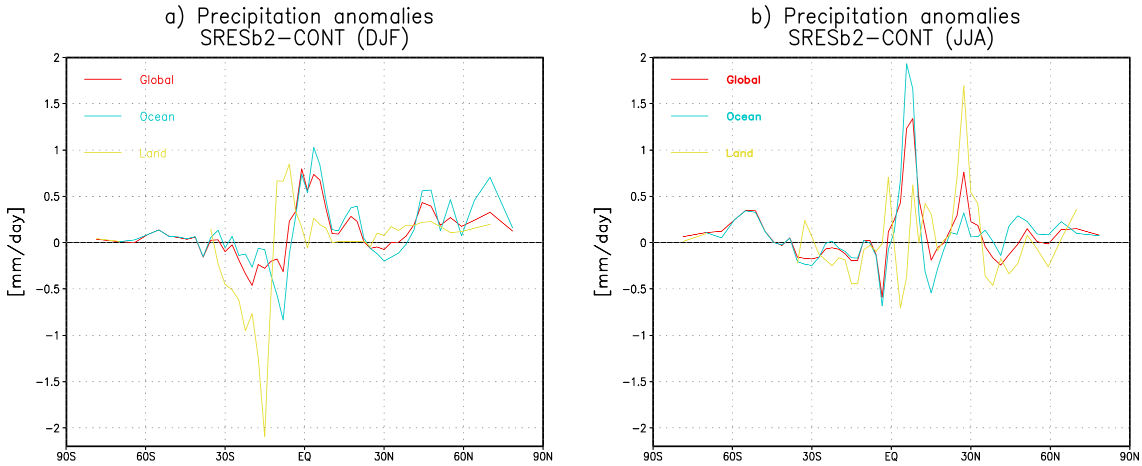

Figure 4.10: Zonally averaged precipitation anomalies (mm/day). Panel a displays the December-January-February mean in global mean (red curve), over the oceans (blue), and over land (yellow). Panel b is similar but for June-July-August. The SRESb2 and CONT simulation results have been averaged over the last 5 years (2095-2099) prior to computing their difference.

Conversely, evaporation depends on the amount of water stored in the ground, which is influenced by precipitation. Therefore, if rainfall decreases, less water is available for evaporation, and consequently it is reduced. In brief, less precipitation reduces evaporation which further reduces precipitation. This explains the correlation between the positive (or negative) anomalies of precipitation and evaporation over land.

Figure 4.10 gives two other informations: the ***meridional distribution*** of precipitation and its ***seasonal variability*** at the end of the SRESb2 experiment (2095-2099). Precipitation is stronger mainly in the ITCZ as a result of the intensification of the upward transport of humidity by the Hadley cells (see section 4.1.2.1). The rainfall is enhanced especially over the Pacific Ocean and also over the Atlantic Ocean in June-July-August (JJA). The intense precipitation zone simulated in the CONT simulation over the Indian Ocean near 5°N is reduced in the SRESb2 experiment, leading to the negative peak at this latitude in figure 4.10. During the Southern Hemisphere summer (December-January-February), heavy convective precipitation occurs in the CONT simulation over the continents near 15°S (see chapter 3). The SRESb2 experiment forecasts a reduction of this precipitation peak over all continents (Africa, Australia, and South America). In JJA, the monsoon brings more rainfall over China, Myanmar, and Thailand. At mid-latitudes, the winter is wetter especially over the ocean but also over the Northern Hemisphere continents. On the contrary, the mid-latitude summer is dryer over the US, Western Canada, Europe and most of Asia.

Among all these modifications of the precipitation patterns, only the increase in the mid- and high latitudes in winter is ***significant*** in zonal mean (figure 4.11a). Indeed, the interannual variability in the tropics is so important that only very large increase of rainfall exceeds the confidence level. Evaporation increases everywhere except over the Southern Ocean where the surface warming is very small (figure 4.11b). In fact, evaporation depends

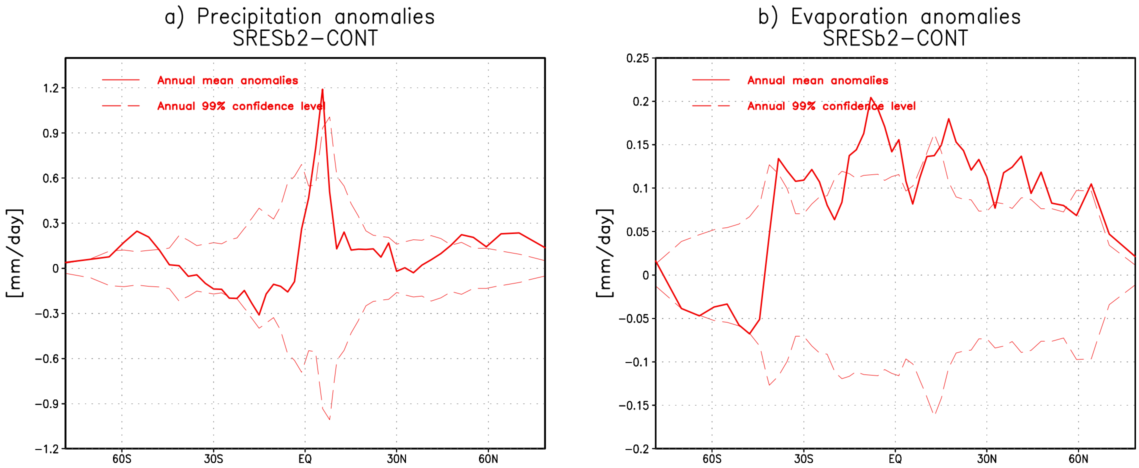

Figure 4.11: Zonally averaged precipitation (panel a) and evaporation (panel b) anomalies (mm/day) between the SRESb2 experiment and the CONT simulation. The SRESb2 and CONT simulation results have been averaged over the last 5 years (2095-2099) prior to computing their difference. The dashed lines are the 99% confidence level computed as 2.33 times the standard deviation from the CONT simulation.

on the saturation level of the surface air. As the surface air temperature increases (see section 4.1.1.1), more humidity is needed to reach saturation. Consequently, evaporation increases. Furthermore, as the Hadley cells are more intense, the water vapour provided to the atmosphere by evaporation at the surface is rapidly transported upwards. This intensification of evaporation is significant between 40°S and 50°N, more precisely, between 40°S and the equator in June-July-August, and between 15°N and 50°N in December-January-February. The winter hemisphere Hadley cell is indeed more intense than the one of the summer hemisphere.

As for the surface air temperature change, the IPCC Third Assessment Report (*Cubasch et al.* [2001]) provides information on the ***horizontal patterns of the precipitation change*** forecasted using the SRES B2 scenario in various coupled models (figure 4.12b). Precipitation shows a high inter-model variability and therefore little consistency among models. It is therefore more difficult to estimate the "quality" of the LMD5-CLIO2 results. Rainfall in the ITCZ increases in the SRESb2 simulation as in the multi-model ensemble mean. Nonetheless, the intensification of precipitation over Indonesia forecasted by LMD5-CLIO2 is stronger than in the multi-model mean. This feature seems specific to our experiment. The same remark holds for the increase of rainfall over India and South-East Asia. Correlated to the high temperature increase over the Southern Hemisphere continents, precipitation is reduced over South America, over the western part of Africa, and over Australia. Over North Africa, the multi-model ensemble mean predicts an increase in precipitation around 15°N and a decrease over North Sahara. In the SRESb2 simulation, the contrast is less meridional but more zonal: decrease of precipitation in the western part and increase in the eastern one, and again a reduction of rainfall over the Middle East region. Due to all these discrepancies, the prediction of LMD5-CLIO2 seems very different than the multi-model ensemble mean. Nevertheless, we should notice that the

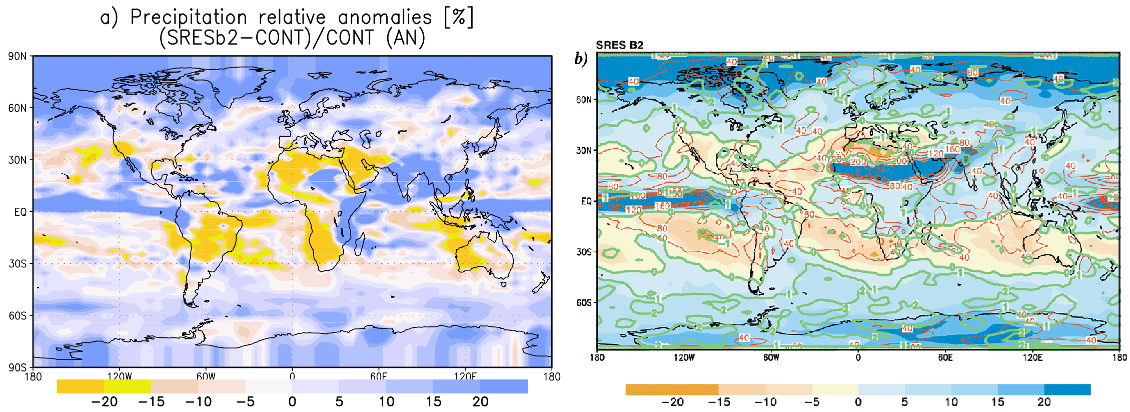

Figure 4.12: Panel a displays the annual mean precipitation changes between the SRESb2 experiment and the CONT simulation (%). The SRESb2 and CONT simulation results have been averaged over the last 5 years (2095-2099) prior to computing their difference. Panel b comes from *Cubasch et al.* [2001] and provides the multi-model ensemble annual mean change of the precipitation (color shading), its range (thin red isolines) (%), and the multi-model mean change divided by the multi-model standard deviation (solid green isolines, absolute values).

consistency between the models contributing to this multi-model mean is very low too. On the contrary, most coupled models agree to forecast a precipitation increase in the mid- and high latitudes. It is also the case of the SRESb2 simulation with an amplitude similar to the multi-ensemble mean.

Looking more precisely over Africa, we notice that precipitation is reduced in the western part and enhanced in the eastern part, especially near the source of the Nile in June-July-August and over Tanzania. Consequently, evaporation is modified as respectively less or more water than in the CONT simulation is available. These changes in the rainfall besides influences the ***runoff***. The runoff of the main rivers is given in table 4.1 for the end of the SRESb2 simulation. The African rivers flowing into the Atlantic Ocean (namely Congo and Niger) carry less freshwater, while the Nile brings more freshwater towards the Mediterranean Sea and the Indian Ocean also receives more freshwater from the African continent. In the center of the US, the amount of rain is strongly reduced in summer and slightly enhanced in winter. These modifications lead to a reduction of the water carried by the Mississippi towards the Gulf of Mexico and consequently into the Atlantic Ocean. In South America, the flow of the major rivers bringing water to the Atlantic Ocean (namely Amazon and Parana) is also reduced. It is not a straightforward response to a reduction of precipitation throughout the year. Precipitation is enhanced during December-January-February near the equator and reduced southwards. During the opposite season (June-July-August), precipitation is reduced over the whole South American continent except over Peru and Ecuador along the western coast. As a consequence there is an obvious decrease of the freshwater runoff towards the Atlantic Ocean. After this inventory of the main locations where the continental runoff decreases in the SRESb2 experiment compared to the CONT simulation, we indicate the rivers whose flow increases.

River	CONT	SRESb2	SRESb2-CONT
Amazon	5699	4226	-1473
Brahmaputra and Ganges	2040	2808	+768
Congo	4347	3536	-811
Mekong	555	1049	+494
Yangtze and Xi	1868	2096	+228
Mississippi	1349	1201	-148
Niger	2084	1747	-337
Parana	764	596	-168
Orinoco	730	722	-8
Amur and Yellow	979	955	-24
Nile	861	979	+117
Zambezi	386	415	+29
Murray	283	261	-21
Indus	317	396	+79
Lena and Yana	326	390	+64
Yenisey	368	444	+75
Ob	290	312	+21
Saint Lawrence River	504	566	+62
Western Dvina	133	160	+27

Table 4.1: Annual river discharges in km^3/year. LMD5-CLIO2 results are averaged over the last 5 years (2095-2099) for both the SRESb2 and CONT simulations, prior to compute their difference. In the forth column, the significant increase are in red, the negative anomalies are i blue. Rivers flowing to the Atlantic Ocean are in green. Arctic rivers are in light blue.

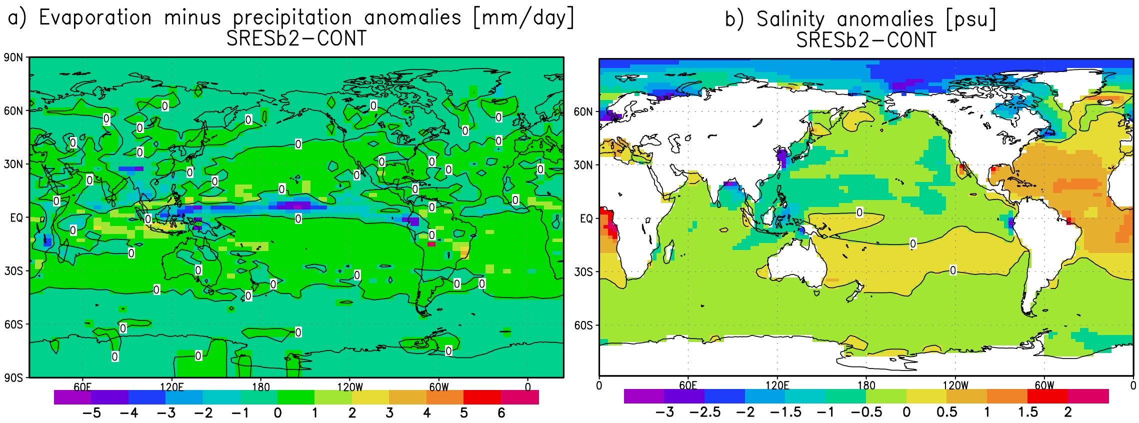

Figure 4.13: Annual mean anomalies between the CONT simulation and the SRESb2 experiment. The oceanic surface salinity anomalies (psu) are shown in panel a, and the evaporation minus precipitation anomalies in panel b (mm/day). The SRESb2 and CONT simulation results have been averaged over the last 5 years (2095-2099) prior to computing their difference.

As previously explained, more freshwater arrives in the Mediterranean Sea and in the Indian Ocean transported by the African rivers. The increase of precipitation throughout the year over Peru brings more water into the Pacific Ocean. Over Southeast Asia, the intensification of the summer monsoon over China, Thailand, and Myanmar increases the flow of Brahmaputra, Ganges, Yangtze, and Mekong. Finally, more convective precipitation over Indonesia leads to an intensification of the river runoff in this region.

4.1.2.3 Oceanic salinity changes

Different aspects of the hydrological cycle give their fingerprint on the surface-salinity field in the ocean (figure 4.13b). First, the melting of the ice pack in the Arctic basin (see section 4.1.4) releases freshwater at the top of the Arctic Ocean. The surface salinity is therefore reduced by up to 2.5 psu. Elsewhere, precipitation and evaporation both influence the surface salinity (figure 4.13a), without forgetting the continental runoff. In the Pacific Ocean, freshening is forecasted in the ITCZ due to the increase of convective precipitation (see above). Southwards around the Tropics of Capricorn, the intensification of the Hadley cells leads to higher evaporation and consequently to higher surface salinity. This should also be the case in the Northern Hemisphere: indeed, evaporation increases more than precipitation in this zone. Nonetheless, the salinity signal is altered by the runoff. The amount of freshwater discharged by the rivers is enhanced by stronger precipitation over China during the monsoon (June-July-August) and over Indonesia. The high salinity anomalies forecasted by the SRESb2 simulation in the Atlantic Ocean are caused by three factors: the increase of evaporation, the reduction of precipitation in the Southern Hemisphere, and the reduction of the continental runoff from Africa and South America. This last factor seems significant to explain the difference between the Atlantic and the Pacific Oceans. All these anomalies are restricted to the upper ocean (the first $200 - 400$ m). Below, no significant change is simulated by LMD5-CLIO2 in the SRESb2

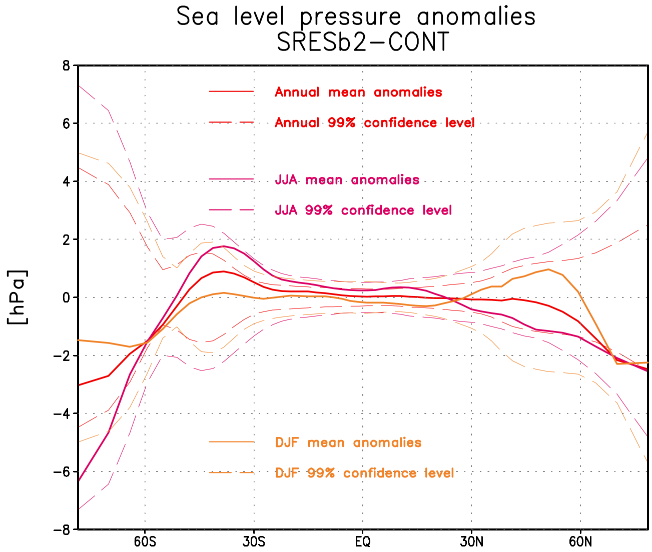

Figure 4.14: Zonal mean sea-level pressure (hPa) as simulated by the SRESb2 simulation compared to the CONT experiment (averaged over the last 5 years 2095-2099). The solid lines are the anomalies forecasted by LMD5-CLIO2 at the end of the SRESb2 simulation in annual mean (red curve), during boreal summer (JJA, magenta curve), and during Southern Hemisphere summer (DJF, orange curve). The dashed lines are the 99% confidence level computed as 2.33 times the standard deviation from the CONT simulation.

experiment compared to the CONT simulation.

4.1.3 Dynamic response

4.1.3.1 Atmospheric circulation changes

The modifications of the atmospheric circulation are not very significant at the end of the 21st century. The zonally averaged seasonal means of the sea-level pressure do not show any significant change neither in December-January-February (DJF) nor in June-July-August (JJA) (figure 4.14). Nonetheless, it seems that the winter-hemisphere pressure gradient between the mid-latitude high pressures and the high latitudes low pressures tends to increase. Indeed, in the Northern Hemisphere in DJF, the anticyclones located over the Asian continent extend further north towards Russia, and the high pressure simulated by LMD5-CLIO2 over the Pacific Ocean near 35°N expands to the east towards America. Concurrently, the sea-level pressure over the Barents and Kara seas is reduced. Similarly, the low pressure surrounding Antarctica is deeper in the SRESb2 simulation compared to the CONT experiment in JJA, and the high pressures located over the oceans are stronger and their southward extension is shifted slightly further towards Antarctica. During the same season, the summer low pressure over Asia undergoes a significant change: the sea-level pressure is reduced eastward of the Caspian Sea over Ousbekistan, Turkmenistan, and Afghanistan.

When comparing the results of the SRESb2 simulation to the multi-model ensemble

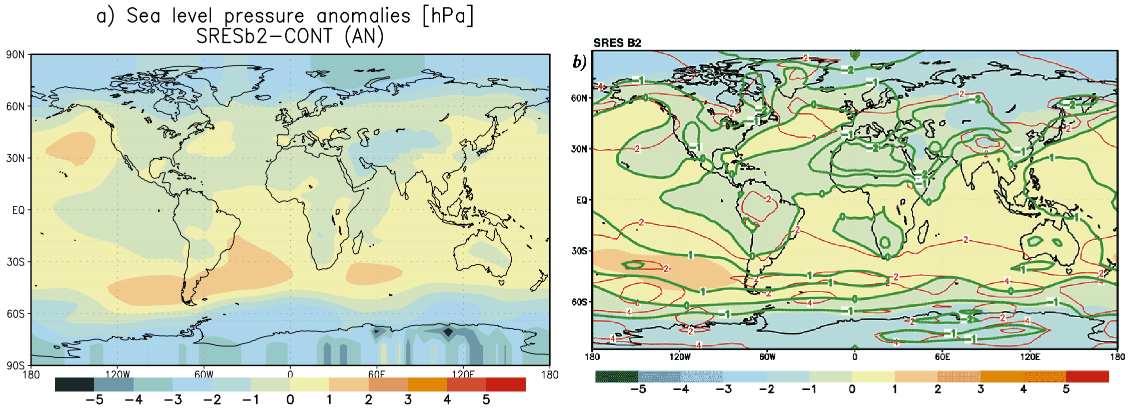

Figure 4.15: Panel a displays the annual mean sea-level pressure anomalies between the SRESb2 experiment and the CONT simulation (hPa). The SRESb2 and CONT simulation results have been averaged over the last 5 years (2095-2099) prior to computing their difference. Panel b is taken from *Cubasch et al.* [2001] and provides the multi-model ensemble annual mean change of the sea-level pressure (color shading), its range (thin red isolines) (hPa) and the multi-model mean change divided by the multi-model standard deviation (solid green isolines, absolute values).

mean computed by the IPCC (*Cubasch et al.* [2001]), similarities appear (figure 4.15). The sea-level pressure tends to decrease over land and to increase over ocean in both cases. The important intensification of the low pressure located over the Arctic region forecasted by LMD5-CLIO2 (up to -3 hPa) has an amplitude close to the multi-model ensemble mean. The reduction of the sea-level pressure over North Africa, the Middle-East region, and central Asia is also a consistent feature shared by many models (the multi-model mean change divided by the multi-model standard deviation exceeds two). In our simulation, the stronger sea-level pressure rise is located in the Southern Hemisphere mid-latitudes in good agreement with the IPCC report. Nonetheless, the precise location of this increase differs between the SRESb2 experiment results and the multi-model ensemble mean.

Before studying the oceanic circulation changes, it is interesting to estimate the impact on the surface wind stress of the enhanced greenhouse effect combined to the direct sulphate-aerosol effect. The surface oceanic currents are indeed driven by the stress performed by the wind on the sea surface. The zonal wind stress anomalies averaged zonally are shown in figure 4.16 in annual mean but also seasonally; the significance levels are also drawn. These anomalies are not significant at 99% level neither in December-January-February (DJF), nor in June-July-August (JJA). Nevertheless, intensification of the westerly winds in the Southern Hemisphere mid-latitudes is obvious throughout the year. Consequently, the annual increase is significant. The intensification of these winds is furthermore consistent with the stronger sea-level pressure gradient at these latitudes (see above). Another strong modification of the zonal wind stress occurs in DJF around 65°N. The westerlies are more intense over the North Atlantic Ocean, but this anomaly is not relevant taking into account the CONT run variability.

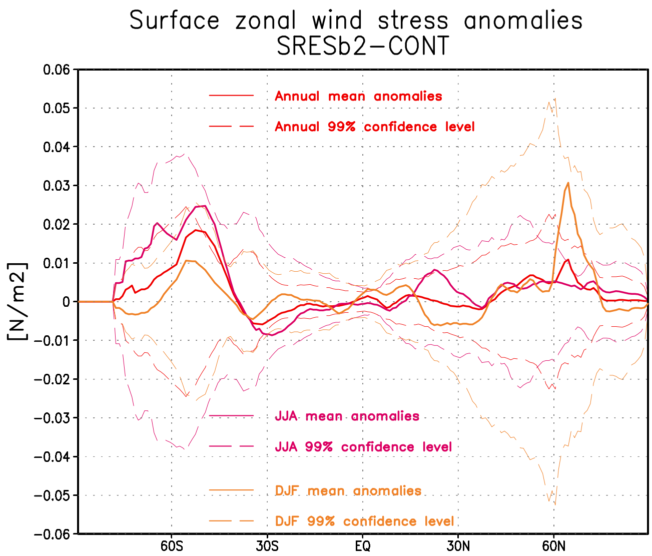

Figure 4.16: Zonally averaged zonal surface wind stress (N/m^2) as simulated by the SRESb2 simulation compared to the CONT experiment (averaged over the last 5 years 2095-2099). The solid lines are the anomalies forecasted by LMD5-CLIO2 at the end of the SRESb2 simulation in annual mean (red curve), during boreal summer (JJA, magenta curve), and during Southern Hemisphere summer (DJF, orange curve). The dashed lines are the 99% confidence level computed as 2.33 times the standard deviation from the CONT simulation.

4.1.3.2 Oceanic current modifications

As no significant modification of the atmospheric circulation has been detected. The surface mixed-layer oceanic circulation is expected to undergo little change in the SRESb2 experiment compared to the CONT simulation. The surface cells of the meridional streamfunction, which are forced by the atmospheric wind stresses, are similar in both simulations and in all basins as shown in figure 4.17. The only visible change is the slight deepening of the Deacon cell in the Southern Ocean. Indeed, the 5 Sv curve is located at about 850 m deep in the CONT run, whereas it reaches 1225 m in the SRESb2 experiment at the end of the 21st century. Concurrently, the maximum overturning rate of this cell raises from 26.6 Sv to 29.2 Sv. This modification is probably associated to the intensification of the westerlies over the Southern Ocean.

In contrast to the surface oceanic circulation, the thermohaline circulation undergoes relevant changes. This is not surprising as the thermohaline forcing anomalies (thermal and hydrological changes) are significant.

The NADW formation is reduced, leading to a decrease of the maximum overturning rate in the North Atlantic Ocean from 13.1 Sv in the CONT simulation to 11.3 Sv in the SRESb2 experiment at the end of the 21st century (figure 4.17c and d). Two factors can improve the stability of the oceanic water column: a surface warming or a surface freshening. To investigate this question, the surface heat and water fluxes have been integrated over all the North Atlantic Ocean from 50°N to 80°N and from 60°W to 30°E at the end of the simulation (2095-2099). The freshwater flux increases by 0.0254 Sv in the SRESb2 simulation compared to the CONT run. Most of these change are associated to modifications of the sea-ice melting areas and to the increase of the Iceland runoff (the Greenland freshwater discharge is held constant in these simulations). The North Atlantic Ocean also releases less heat into the atmosphere: 28.7 $\mathrm{Wm^{-2}}$ instead of 30.3 $\mathrm{Wm^{-2}}$ in the CONT simulation. Consequently, the surface layer tends to be warmer and vertical stability is improved.

In the other hemisphere, around Antarctica, the production of AABW also slows down (figure 4.17). Consequently, the export of AABW over the floor of the three oceanic basins decreases. The amount of AABW entering the Atlantic Ocean at 35°S undergoes a reduction of 2.2 Sv . In the Indian and Pacific Oceans, the AABW inflow is also weaker (−3.2 Sv). Deep convection occurs southwards of 60°S. In this region, the freshwater budget at the surface of the ocean increases by 0.17 mm/day in the SRESb2 experiment compared to the CONT simulation, enhancing the vertical stability of the water column. Another contribution to the stabilization comes from heat fluxes. More energy is received by the ocean at its top: the averaged surface flux anomaly over this region reaches 7.4$\mathrm{Wm^{-2}}$ when the SRESb2 and CONT simulations are compared at the end of the 21st century.

4.1.4 Sea-ice response

The Arctic sea ice undergoes an important melting over the 21st century. The thawing of sea ice is obvious on the time evolution of the ice-pack volume (figure 4.18). The decrease is almost linear with a slope of about $-202.6\ \mathrm{km^3/y}$ i.e. about $-177\ \mathrm{km^3}$ of water/y $\simeq -5.6 \times 10^{-3}$ Sv. The disappearance of sea ice implies both a reduction of the ocean surface covered by sea ice ($-20.6 \times 10^3\ \mathrm{km^2/y}$) and a thinning of the sea-ice layer (-1.1 cm/y).

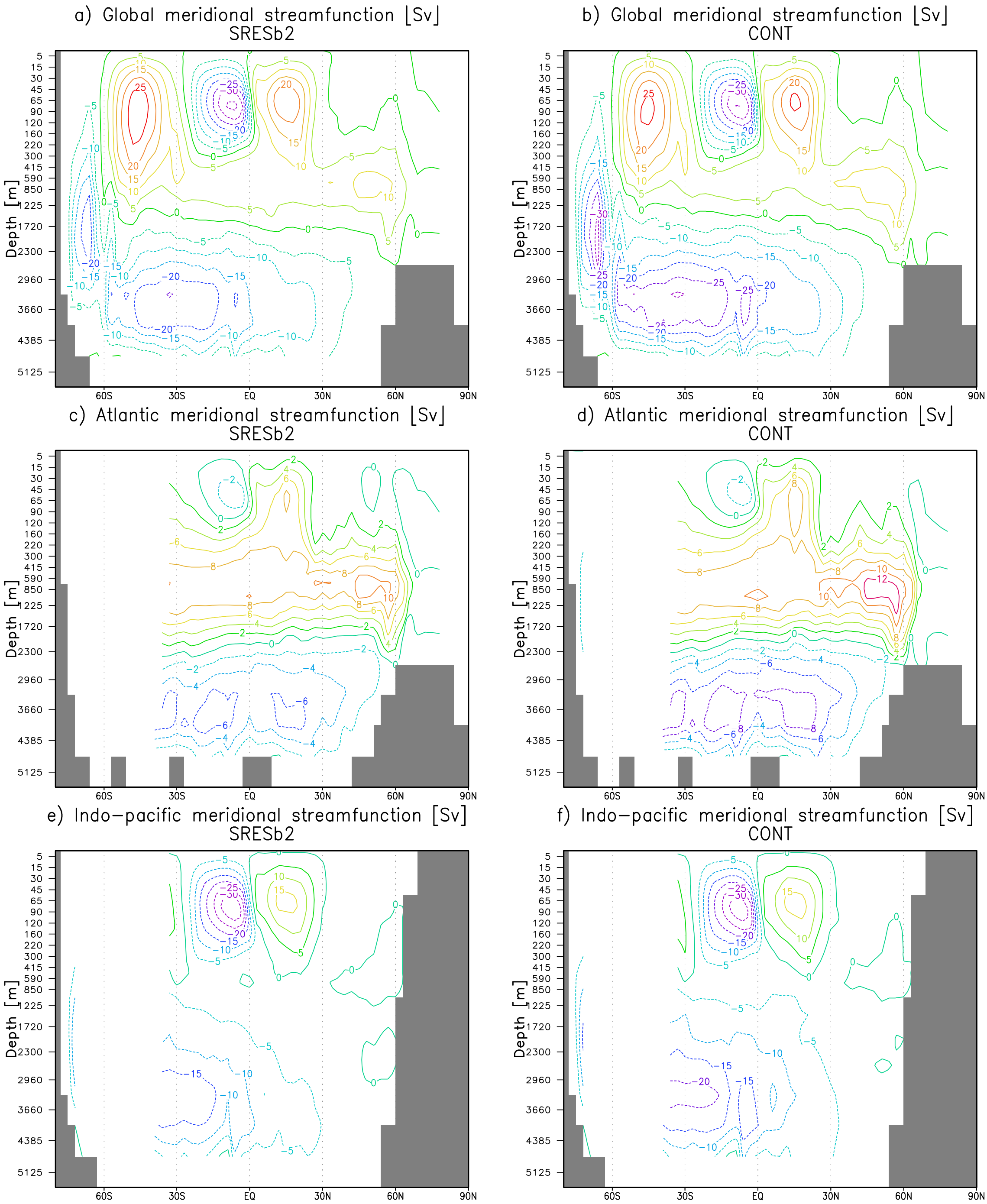

Figure 4.17: Meridional overturning streamfunctions (Sv) as simulated by the SRESb2 simulation (on the left) and the CONT experiment (on the right). These results have been averaged over the last 5 years 2095-2099. The upper panels show the global streamfunction, the middle ones display the Atlantic streamfunction, and the bottom ones the Indo-Pacific streamfunction.

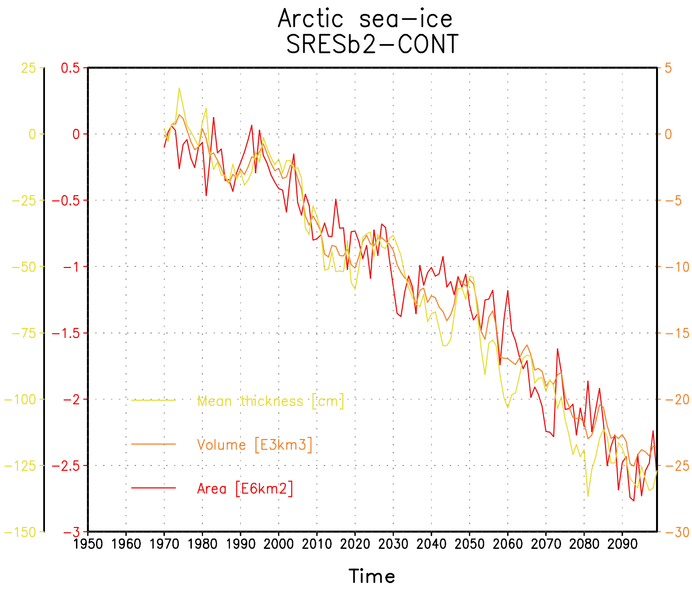

Figure 4.18: Time evolution of the Arctic sea ice. This figure shows anomalies between the SRESb2 and CONT simulations. The sea-ice volume is plotted in red, the sea-ice area in orange and the mean sea-ice thickness (the ratio of the previous ones) in yellow.

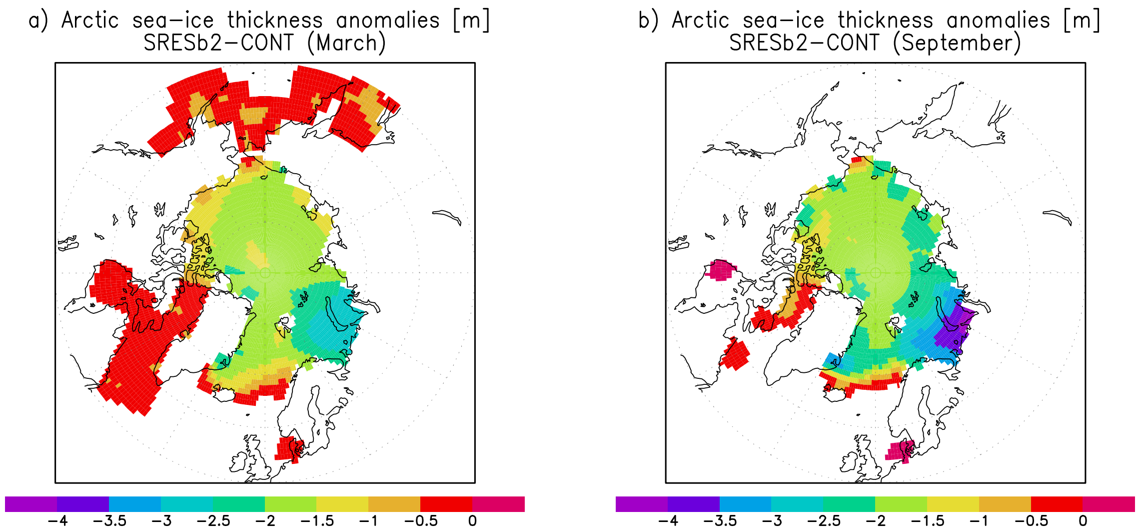

Figure 4.19: Arctic sea-ice thickness anomalies at the end of the 21st century (2095-2099) as simulated in the SRESb2 simulation. The extreme seasons (March and September) are both displayed.

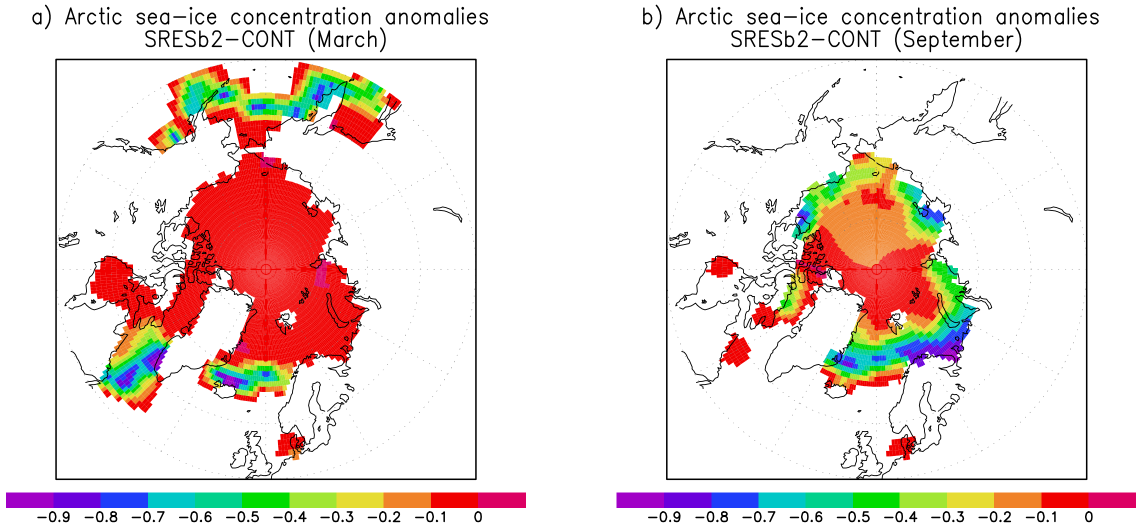

Figure 4.20: Arctic sea-ice concentration anomalies at the end of the 21st century (2095-2099) as simulated in the SRESb2 simulation. The extreme seasons (March and September) are both displayed.

The reduction of the sea-ice thickness is not uniform in space and over the seasonal cycle (figure 4.19). Near the sea-ice margin, sea ice is thin in the CONT simulation. So, complete disappearance of sea ice in this region is not associated to a strong signal in the thickness field. The main decrease occurs in the Barents and Kara Seas where up to 4 m melt in summer (September) and about 3 m in winter (March). Elsewhere in the Arctic basin, the sea-ice thinning is around 1.5 m. Nonetheless, the thickness pattern remains similar in the SRESb2 simulation as the one in the CONT simulation, with a maximum located north of Greenland.

Inside the ice pack, leads expand (with a small positive trend of +838 km^2/y). The parameterization of the ablation of sea ice in LMD5-CLIO2 (see chapter 2) implies that the variation of the concentration is proportional to the relative change in thickness. It means that if sea ice is thicker, a greater thinning would be needed to imply the same change in the concentration. As a consequence, the concentration decrease is less important in the center of the Arctic basin than near the sea-ice margin (figure 4.20).

Due to these two factors, the sea-ice cover becomes less efficient to insulate the ocean from the atmosphere. To investigate the link between sea-ice melting and the heat fluxes, the surface heat fluxes are examined. While their analysis brings information on the processes that imply the sea-ice melting, one should keep in mind that atmospheric conditions can change due to non-local mechanisms and alters sea ice.

Figure 4.21a illustrates the surface heat-flux anomalies computed by LMD5-CLIO2 ***at the sea-ice margin*** in the North Atlantic Ocean. First, the *ice/albedo feedback* is obvious. The partial disappearance of sea ice reduces the surface albedo as ice-covered areas with a high albedo are replaced by open-water areas. Consequently, more solar radiation is absorbed at the surface. At these high latitudes, the incoming solar radiation exhibits a strong seasonal cycle (zero in winter and very strong in summer). The impact of the solar

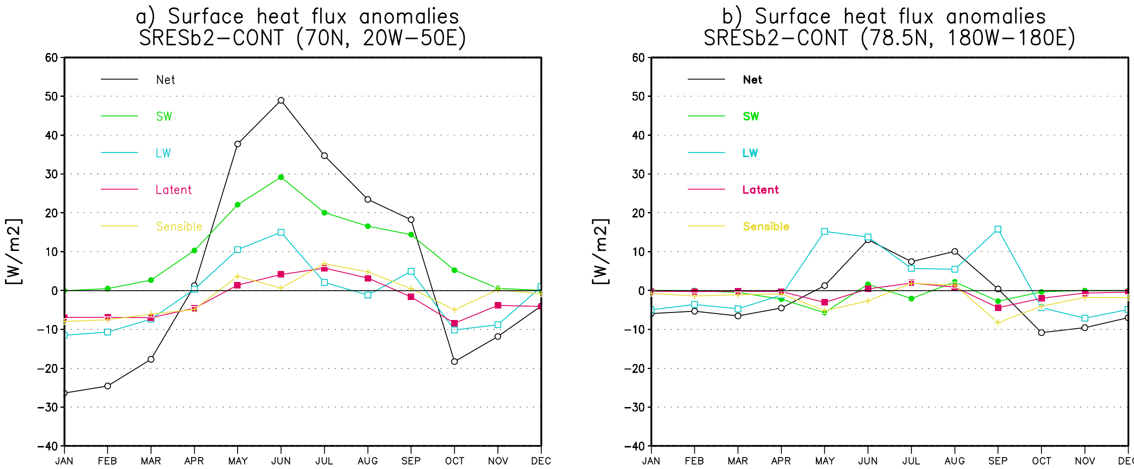

Figure 4.21: Seasonal cycle of the surface heat flux anomalies during the last 5 years of the simulation (2095-2099). The anomalies are computed as differences between the SRESb2 and CONT simulations. The net surface heat flux is in black, the shortwave heat flux in green, the longwave heat flux in yellow, the latent heat flux in red, and the sensible heat flux in cyan. All these fluxes are positive downwards. On panel a, these are averaged at latitude 70°N from the eastern Greenland coast to the Barents sea (20°W to 50°E). Panel b shows the same for the center of the Arctic basin (78.5°N, all around the Earth).

radiation is thus maximum in summer. Secondly, the net longwave radiation also provides more energy to the surface. As the surface temperature increases, Stefan-Boltzman's law implies that more longwave energy is emitted upwards but as the atmosphere contains more greenhouse gases including water, this upward radiation is more efficiently trapped and re-emitted back to the surface. It seems that the main contribution comes from changes in the low level clouds. The water-vapour concentration increases in the atmosphere as its temperature increases (Clapeyron's law) and as open-water area evaporates more than ice-covered area. The air is thus closer to saturation and condensation occurs. Both cloud fraction and cloud liquid water content increase near the surface trapping more longwave radiation. The net effect of all these changes in the longwave radiation is that the surface cooling by longwave radiation is less efficient. This process is called the *water feedback*.

A reduction of the ice thickness is visible in figure 4.19 ***at higher latitudes near the North Pole***. There, the *ice/albedo feedback* is negligible (figure 4.21b) as the sea-ice melting reduces the thickness but has a small impact on the concentration. On the other hand, the *water feedback* is efficient in summer and especially in May and September. In fact, the warm season is longer in the SRESb2 simulation than in the CONT simulation. Consequently, at the beginning and at the end of this season (May and September), the increase of the air temperature is important and it implies a strong increase of the atmospheric humidity in the low layers of the atmosphere. The cloud fraction and liquid water content are thus enhanced and more longwave radiation emitted by the surface is trapped in the low layer, warming the surface.

Finally, while these two feedbacks occur in summer, the maximum temperature anomalies take place in winter (see section 4.1.1). We will try to explain this apparent inconsistency.

1. What can influence the surface temperature and consequently the surface air temperature over the sea-ice pack ? Both thickness and concentration are important. First, the sea-ice surface temperature over thick ice can fall down in winter to $-40°$C, while the underlying ocean remains at about $-2°$C (the oceanic water freezing temperature). Sea ice is indeed able to support such a strong temperature difference if it is thick enough. According to its conductivity, a few meters are sufficient. Secondly, the surface temperature is almost a surface-weighted average between the open-water temperature and the sea-ice temperature.

2. What happens when the sea-ice pack is reduced thanks to the summer feedbacks ? On the one hand, its thinning brings its surface temperature closer to the freezing point. On the other hand, the open-water surface increases and its contribution to the "mean surface temperature" is bigger. Both effects lead to the warming of the surface and to the rise of the surface air temperature.

3. What explains the difference in the surface air temperature between winter and summer ? In summer, the sea-ice surface temperature is closer to the water freezing point ($0°C$) as sea ice thaws out in both simulations (SRESb2 and CONT). Furthermore, concentration changes induce small modifications in the mean temperature, as the sea-ice surface temperature and the open-water surface temperature are close to each other. On the contrary, in winter, the sea-ice surface temperature differs much more between the SRESb2 and CONT simulations (due to change in thickness) and the increase of lead area has a stronger impact during this season. The surface air temperature anomalies is thus smaller in summer than in winter over the Arctic basin.

4. Furthermore, the winter atmosphere is much more stable than the summer one. Consequently, atmospheric convection occurs in summer. It spreads the surface warming into the upper atmospheric layers. Conversely, in winter the warming is confined near the surface. Thus, this process furthers strong surface changes in winter and smaller ones in summer.

4.1.5 Conclusion

Most of the results of the SRESb2 simulation corroborate those obtained with other AOGCMs: global warming, stronger temperature increase over continent than over ocean, intensification of the warming in Arctic, amplification of the hydrological cycle with more precipitation, more evaporation and increased specific humidity in the atmosphere. The main river runoff is also altered. All this modifies the surface salinity in the ocean. The dynamic response is not marked in the atmosphere and in the oceanic surface circulation. However, the oceanic thermohaline circulation is reduced in the Atlantic ocean due to temperature and precipitation changes. The strength of the sea-ice melting in Arctic is not often studied. An attempt is make above to illustrate the main feedbacks that induces this reduction of the sea-ice pack.

In the SRESb2 experiment, the Greenland ice-sheet freshwater flux is kept constant. The rest of this chapter is devoted to the analysis of the SRESb2G simulation in which the Greenland ice-sheet freshwater flux is interactively computed by the GISM. We mainly compared the two climate-change experiments to investigate the potential impact of Greenland on the 21st century climate.

4.2 Implications of freshwater flux from the Greenland ice sheet

While the two climate-change experiments (SRESb2 and SRESb2G) lead to similar results until 2075, they diverge during the last 25 years. As the only difference in the forcing is the Greenland runoff and calving, the explanation is searched in this direction. The anomalies between SRESb2 and SRESb2G are indeed not due to variability, the difference between the two simulations (e.g. on surface temperature, sea-ice volume) is significant at a level of 95%. The most spectacular modification is the shutdown of the deep convection in the North Atlantic Ocean. Changes in the thermohaline circulation are therefore first described. Reasons of these changes are then researched and a mechanism is suggested which links Greenland freshwater flux to convection collapse. Finally, the climatic impacts of these changes are presented. These results are also described in *Fichefet et al.* [2003b].

4.2.1 Alterations of the thermohaline circulation

The North Atlantic branch of the thermohaline circulation collapses at the end of the SRESb2G simulation. To document this, three components of this circulation pattern are shown hereafter: the deep-water formation, the northward transport of warm tropical water by the Gulf Stream, and the return southward current at depth.

First, the formation of the NADW could be illustrated by a composite map of the depths of vertical convection as in chapter 3. But, as the time evolution of convection is of key interest to distinguish between the SRESb2 and SRESb2G experiments, two-dimensional latitude-longitude maps are not the most efficient tool. Consequently, the fractions of the North Atlantic zone (defined as the region between 80°W and 20°E, and 30°N and 90°N) where convection reaches 1000 m, 2000 m and 3000 m, respectively, have been computed annually for March. The time evolution of these quantities (figure 4.22) indicates that the convection intensity decreases at the end of the SRESb2G simulation compared to the SRESb2 run. The signal becomes significant at 99% around 2087. The maximum convective depth rapidly decreases from more than 3000 m to about 1800 m. In fact, deep convection disappears near the Greenland coast (where it is located in the CONT simulation, see chapter 3) and shallower convection remains southwest of Iceland (figure 4.23).

The disappearance of the deepest convection in the North Atlantic Ocean alters the thermohaline circulation. The zonal mean meridional streamfunction in the Atlantic Ocean averaged over the last 5 years (2094-2099) (figure 4.24) indicates that dense water formed in the North Atlantic Ocean dives to more than 2500m near 60°N in the SRESb2 experiments, whereas water remains above 1500 m at the same latitude when the Greenland freshwater flux change is taken into account. Southwards, no significant modification is observed as

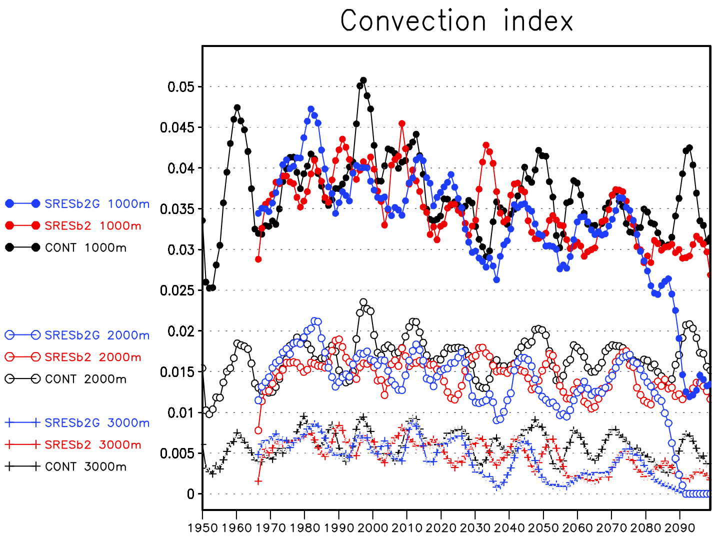

Figure 4.22: Fractions of the North Atlantic zone (defined as the region 80°W − 20°E and 30°N − 90°N) where convection reaches 1000 m, 2000 m, and 3000 m, respectively. These have been computed annually for March in the CONT, SRESb2, and SRESb2G experiments. Furthermore, a 5-year running mean has been applied to smooth out the greatest peaks.

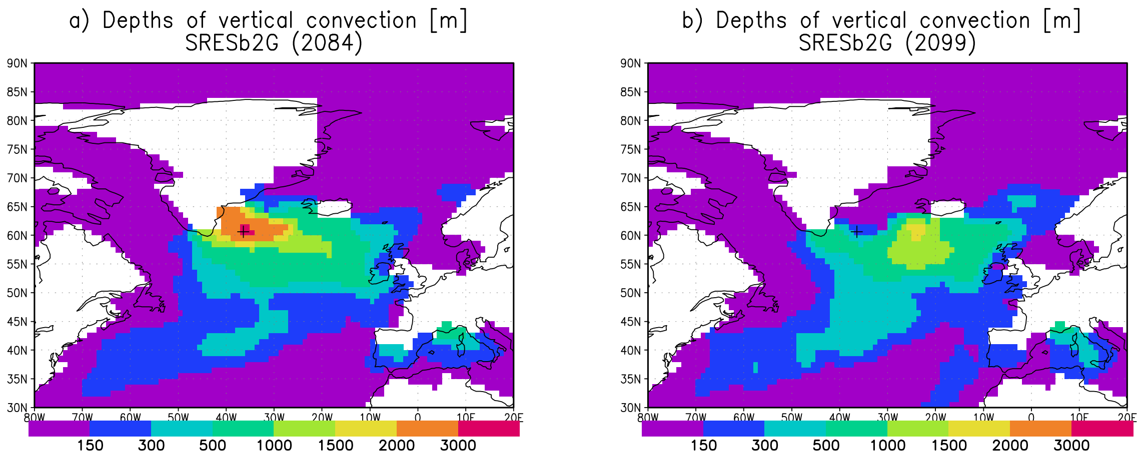

Figure 4.23: Depths of vertical convection (m) in the SRESb2G simulation during March 2086 (panel a) and during March 2099 (panel b). The depth of convection is diagnosed as the depth to which the water column is unstable. Contour levels are drawn at 150 m, 300 m, 500 m, 1000 m, 1500 m, 2000 m, and 3000 m.

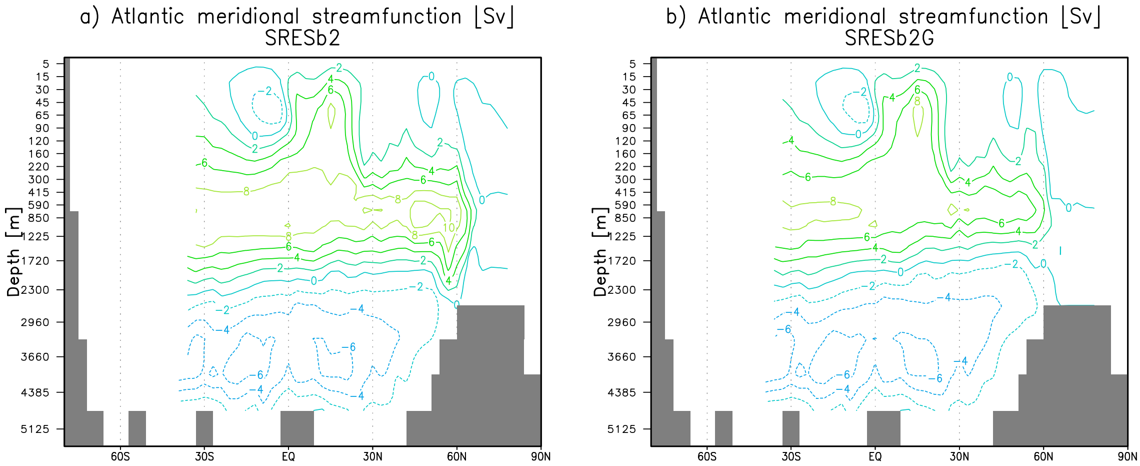

Figure 4.24: Meridional streamfunction (Sv) in the Atlantic Ocean, averaged over the period 2094-2099. The SRESb2 and SRESb2G results are shown respectively on plane a and b.

the deep-water masses did not yet have time to travel so far. Looking at the oceanic motions in horizontal plans at various depths over the 2094-2099 period, the Gulf Stream is slightly less intense near the surface and the North Atlantic Drift, which brings water towards convective regions, is less obvious in SRESb2G. At 850 m, a southward return flow along the North American coast is already obvious in the SRESb2G simulation, while we have to go deeper to see it in the SRESb2 run.

The time evolution of the overturning is displayed in figure 4.25a. An important decrease is forecasted at the end of the SRESb2G simulation. The overturning is also reduced when the impact of the enhanced Greenland water discharge is omitted but no accentuation of this trend is observed at the end of the 21st century. Furthermore, the thermohaline circulation transports heat from the equator to high latitudes (see chapter 1). As a consequence of the reduction of the circulation, the meridional heat transport in the North Atlantic Ocean is weaker in the SRESb2G simulation than in the other two runs (figure 4.25b).

All these elements indicate reduction of the North Atlantic thermohaline circulation in intensity and in depth. Two other questions arise: “why does it change ?”, “what are the climatic impacts of this ?” The first question is tackled in the next section, the second just after.

4.2.2 Why does the oceanic circulation change ?

In the SRESb2 simulation, whereas the North Atlantic branch of the thermohaline circulation decreases, it does not collapse. On the contrary, the deep convection in the high latitude North Atlantic Ocean shuts down at the end of the SRESb2G simulation. As the only difference in their experimental design is the Greenland ice-sheet runoff and calving, we can expect a link between the melting of the Greenland ice sheet and the collapse of the thermohaline circulation. First, the Greenland contribution to the freshwater flux is

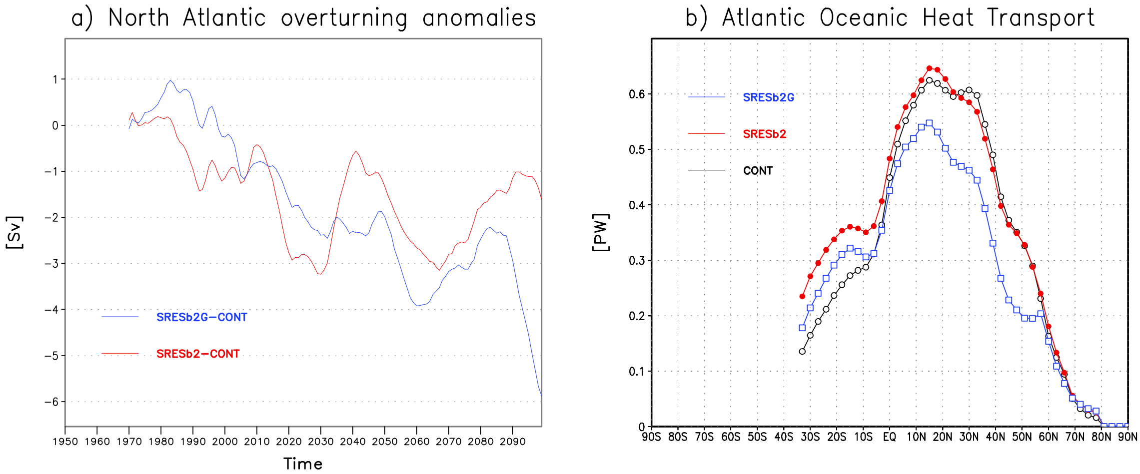

Figure 4.25: a) Time evolution of the overturning in the North Atlantic Ocean (Sv), computed as the maximum of the annual mean meridional streamfunction. The red curve is the difference between the SRESb2 and the CONT simulation, while the blue one is the SRESb2G run compared to CONT. Both have been smoothed by a 10-year running mean. b) Meridional Atlantic heat transport (PW). The CONT, SRESb2 and SRESb2G results are shown for the last five years (2095-2099) in black, red, and blue, respectively.

plotted to get an idea of its intensity. The exceeding freshwater input in the ocean should influence the salinity field and thus the density. These two parameters as well as temperature are thus analyzed near Greenland and in the surrounding of the convective areas: horizontally and vertically.

The starting point of this analysis is the fact that the design of the SRESb2 and SRESb2G experiments is identical except the Greenland runoff and calving. The SRESb2 experiment uses the same freshwater input from the Greenland ice-sheet into the ocean as the one used in the CONT simulation. This freshwater flux has been computed by GISM under present-day conditions. Consequently, this experiment investigates the impact of greenhouse-gas and sulphate-aerosol modifications assuming that the Greenland ice sheet goes on releasing the same amount of freshwater. On the other hand, LMD5-CLIO2 and GISM are coupled in the SRESb2G simulation. As explained in chapter 2, LMD5-CLIO2 provides temperature and precipitation anomalies to GISM, and conversely GISM computes modified runoff and calving from the Greenland ice sheet under perturbed climatic conditions. The SRESb2G experiment therefore takes into account the impact of greenhouse-gas and sulphate-aerosol modifications but also the influence of the Greenland ice-sheet melting.

Figure 4.26a displays the Greenland freshwater flux anomalies during the SRESb2G simulation compared to the CONT and SRESb2 runs, which share the same Greenland water discharge values. GISM computes similar runoff and calving at the beginning of the SRESb2G simulation as in the CONT and SRESb2 runs. The temperature and precipitation anomalies are indeed small during this period. The anomalies then progressively increase following the temperature and precipitation changes. Consequently, the North Atlantic Ocean receives more freshwater flux from the Greenland ice sheet in the SRESb2G

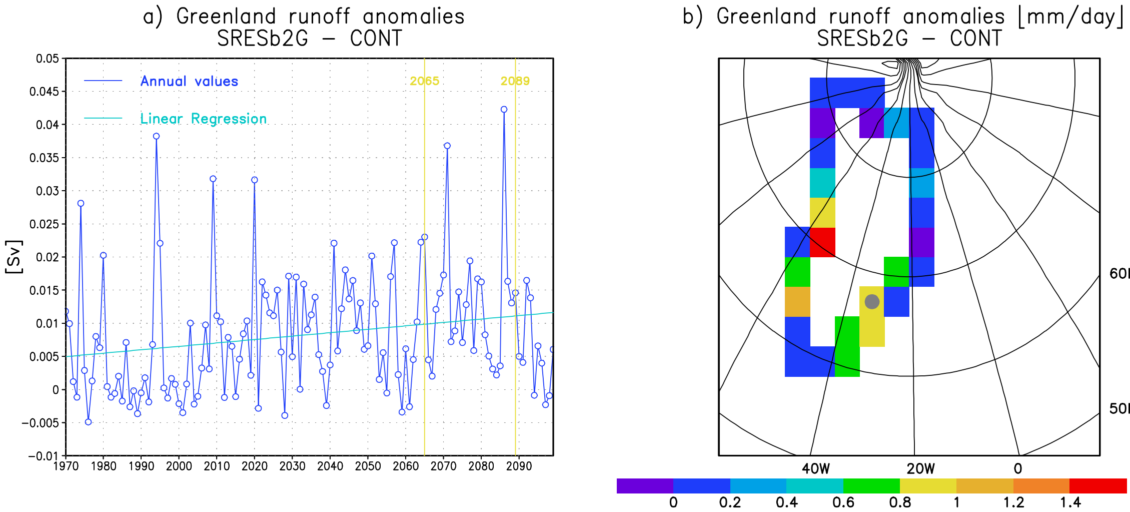

Figure 4.26: Greenland freshwater flux anomalies in the SRESb2G simulation compared to the CONT and SRESb2 experiments. The CONT and SRESb2 values are computed by GISM under present-day climatic conditions. The SRESb2G values are computed by the GISM in response to the temperature and precipitation anomalies forecasted by LMD5-CLIO2 under increasing greenhouse-gas and sulphate-aerosol concentrations. a) Time evolution of the spatial mean. b) Geographical distribution of the time average between 2065 and 2089.

simulation. Furthermore, some major positive peaks occur during the first 50 years and two others near the collapse of the thermohaline circulation (2071 and 2086). The geographical distribution of these anomalies forecasted by GISM between 2065 and 2089 is shown in figure 4.26b. The most important water discharge occurs in the south of Greenland: between 60°N and 70°N along the eastern coast of Greenland and between 65°N and 75°N in the Baffin Bay.

This enhanced freshwater input at the top of the ocean seems to slightly decrease the surface salinity in the Baffin Bay and Greenland Sea. This flux remains too small to strongly influence the salinity in the surface layer. Nonetheless, local freshening can occur especially during year of great Greenland freshwater peaks.

One can bring up against this that the Greenland freshwater discharge is not the only contribution to the surface water budget of the North Atlantic Ocean. Consequently other terms could influence the surface salinity and therefore the thermohaline circulation. To estimate the relative weight of these terms, the water budget at the top of the North Atlantic Ocean (from 50°N to 80°N and from 60°W to 30°E) has been analyzed. For the period 2070-2080, the annual mean surface freshwater flux due to precipitation, evaporation, and river runoff is increased by 0.017 Sv in the SRESb2G experiment compared to the CONT run. At the same time, the Greenland freshwater flux increases by 0.015 Sv. It comes out that Greenland contributes to about 50% of the long-term change in total freshwater flux simulated by LMD5-CLIO2 over this region. Similar conclusions stand for other periods. The Greenland ice sheet is thus a key component to explain the strong reduction of the intensity of the thermohaline circulation in the SRESb2G simulation.

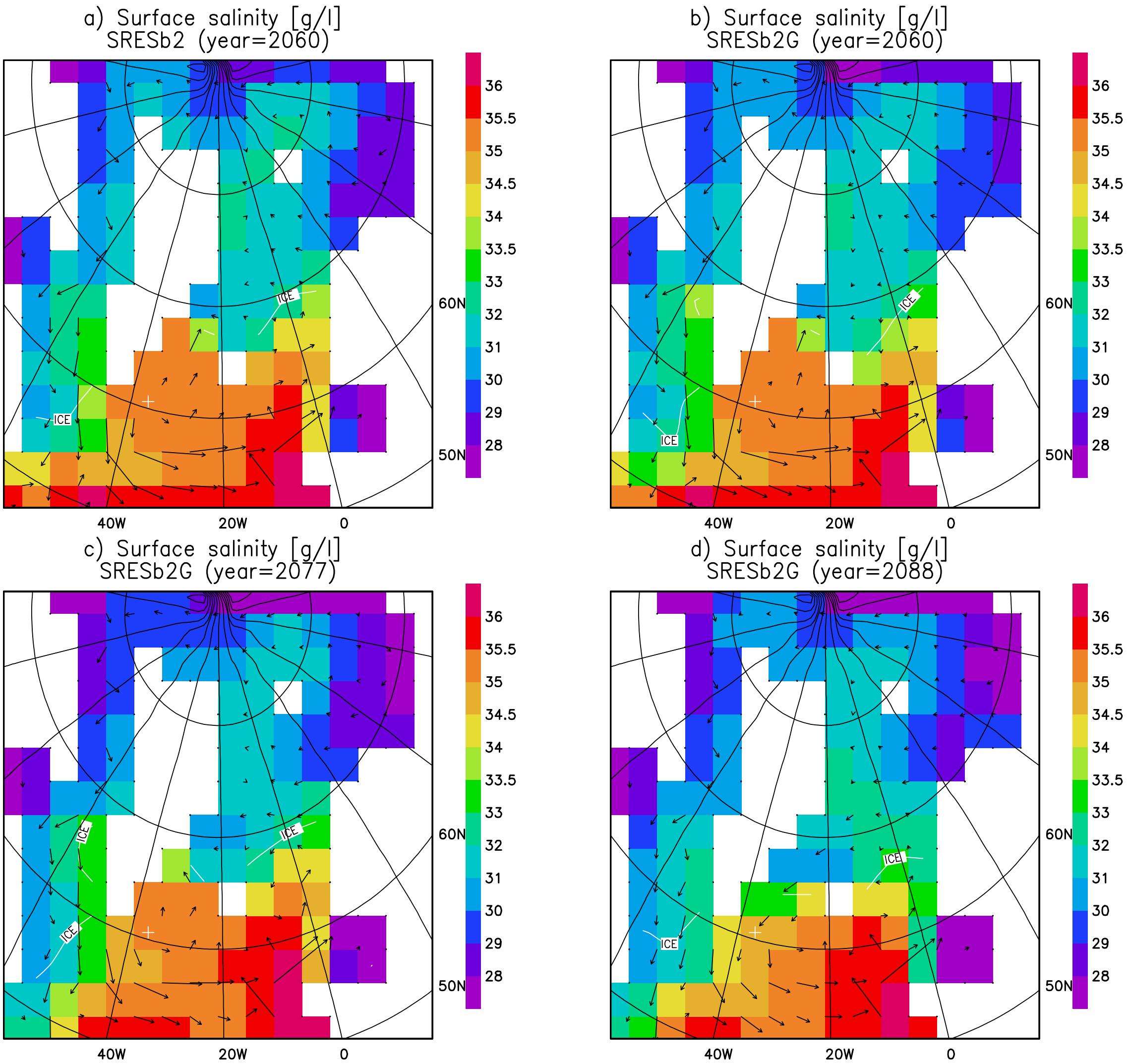

Figure 4.27: Surface salinity (g/l) and surface oceanic velocity in the SRESb2G simulation. Panel a shows annual means for year 2060, panel b for 2077, and panel c for 2088.

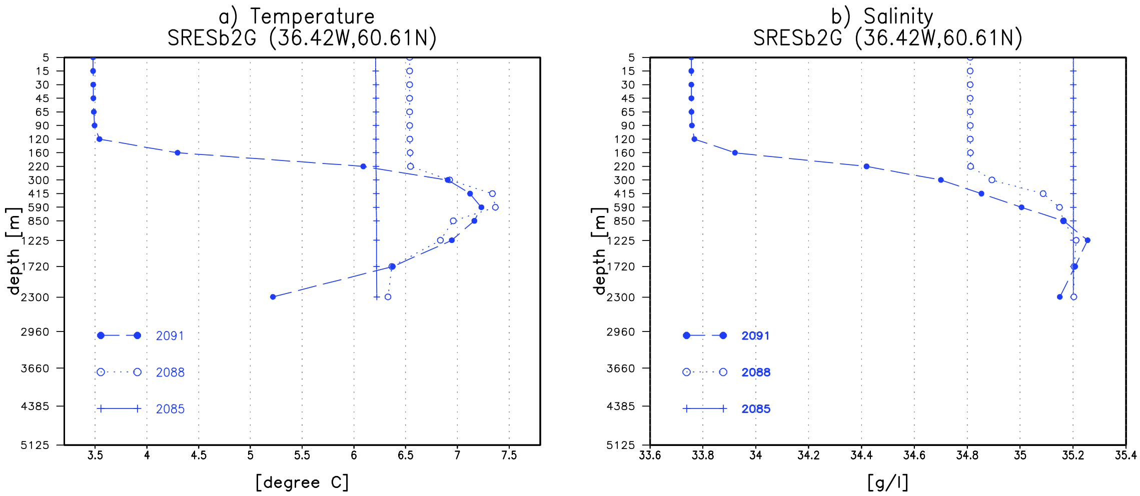

Figure 4.28: March vertical profiles of temperature (panel a) and salinity (panel b) at the model grid point located at (36.42°W, 60.01°N) in the SRESb2G simulation. Three profiles are shown at different years: 2085, 2088, and 2091.

We now focus on the eastern coast of Greenland and on the time slice 2060-2090. We are looking for the parameters that induce the deep-convection shutdown. Convection is driven by local vertical instability. We therefore pay more attention to the salinity and temperature fields south-east of Greenland. Furthermore, the shutdown of the deep convection in the North Atlantic Ocean occurs around year 2087 (see above), time evolutions are thus examined for the 4 preceding decades (2060-2090). The surface salinity and the surface oceanic velocities are displayed in figure 4.27 for three periods, namely 2060, 2077, 2088. Until year 2075, the SRESb2 and SRESb2G simulations share common features around Greenland. Salty and warm water flows northwards in the Denmark Strait (figure 4.27a,b) like in the CONT simulation. A steep salinity gradient is simulated near 65°N, with fresh (32 g/l) and cold water (slightly above the freezing point) northward of a line linking Greenland and Iceland, and with salty (34g/l) and warm water (around 8°C) southwards. This front line agrees more or less with the sea-ice margin. The grid point marked by a grey dot in figure 4.26b (32.62°W, 67.08°N) is located on this boundary. It receives a lot of freshwater from the Greenland ice sheet and its salinity progressively decreases. While its density is reduced, the oceanic current turns westwards (figure 4.27c) probably because geostrophic equilibrium compels the velocity to be parallel to isodensity contours. Indeed, the surface velocity field is influenced by the density gradient, the Coriolis force, and the wind stress. The wind stress remains similar, and sea-ice progressively expanding southwards shelters the ocean from the wind influence. Thus, the oceanic current seems mostly governed by the density gradient and the Coriolis force. This westward current brings fresher water towards the Greenland coast leading to a positive feedback. Finally, as displayed in figure 4.27d, fresh and cold Arctic water flows southwards through the Denmark Strait. Since 2075 until the end of the simulation, a tongue of fresh Arctic water propagates along the eastern coast of Greenland due to oceanic advection. This freshening spreads from 65°N in 2076 to the southern tip of Greenland in 2091.

Figure 4.29: Time evolution of the surface-density anomalies at (36.42°W, 60.01°N) (kg/m^3). The blue curve is the difference between the SRESb2G and SRESb2 simulations. A new density has then been computed using the SRESb2 salinity and the SRESb2G temperature to quantify the influence of temperature changes. The green curve is the difference between this new density and the SRESb2 values. Conversely, the orange curve shows the impact of salinity changes when the SRESb2 temperature and the SRESb2G salinity are used.

We now focus on the convective area. The CLIO2 grid point located at (36.42°W, 60.01°N) marked by a black cross in figure 4.23 convects down to the sea floor until 2087. Afterwards, deep convection shuts down. Vertical profiles of temperature and salinity simulated by LMD5-CLIO2 in March (month of deep convection) confirm this evolution (figure 4.28). Temperature and salinity are initially well mixed from the surface to the bottom of the water column. This is a fingerprint of deep convection. In 2088, a break appears below 300 m. To find the reason of this change, it may be interesting to look at the time evolution of density under the influence of temperature and salinity because convection is governed by the density profile. Density has thus been computed using salinity from the SRESb2 simulation and temperature from SRESb2G to get an idea of the impact of temperature on density, and conversely the SRESb2G salinity and the SRESb2 temperature have been used to quantify the salinity effect (figure 4.29). At the surface (figure 4.29a), the water density seems mainly controlled by salinity. The southward spread of fresh and cold water through the Denmark Strait leads to a reduction of the surface density around 2088 (the reduction by decreasing salinity over-compensates the effect of decreasing temperature). Lighter water at the surface inhibits deep convection, so that the temperature and salinity profiles are well mixed only down to 220 m. Furthermore, when convection collapses, warm water masses located southwards are advected by the horizontal circulation. As long as deep convection mixes the water column, the horizontal velocity field is "altered" by vertical motion. But when this perturbation disappears, the larger scale horizontal advection strongly influences the grid-point salinity and temperature. Consequently, the temperature increases between 300 m and 1225 m. This process explains the break that arises in 2088. The phenomena goes on and the surface salinity and temperature significantly diminish (figures 4.28 and 4.29a), while the "mid-depth" temperature and salinity rise (figures 4.28 and 4.29b). The impacts on density are as follow: decrease near the surface and at "mid-depth". At this point, the density reduction at the surface remains always greater than the one at "mid-depth" so that convection never comes back. Moreover, at greater depths, near the sea floor, density increases after the convection shuts down (figure 4.29c). It seems that AABW (Antarctic Bottom Water) spreads northwards filling space deserted by NADW (North Atlantic Deep Water). As AABW are colder than NADW, temperature decreases at the bottom of the water column. Consequently, heavier water near the bottom inhibits deep convection.

The time evolution of the density profiles are not so straightforward at all grid points. For example (see figure 4.30), southwards at (35.14°W, 57.71°N), the surface density is reduced earlier (2079) by freshwater coming from the Baffin Bay. This inflow is intermittent depending on climate variability. Nevertheless, lighter surface water masses have shut down deep convection. Temperature and salinity are still well mixed above 850 m. At this depth, warm water penetrates by horizontal advection (see above). The impact on density of temperature anomalies are bigger than salinity influence at 850 m (see figure 4.30b), so that density decreases. This sketch mimics what happens at (36.42°W, 60.01°N):

- fresh water inflow near the surface shuts down deep convection;
- at mid-depth (850 m), warm water penetrates from the south;
- so, both the surface and mid-depth densities decrease.

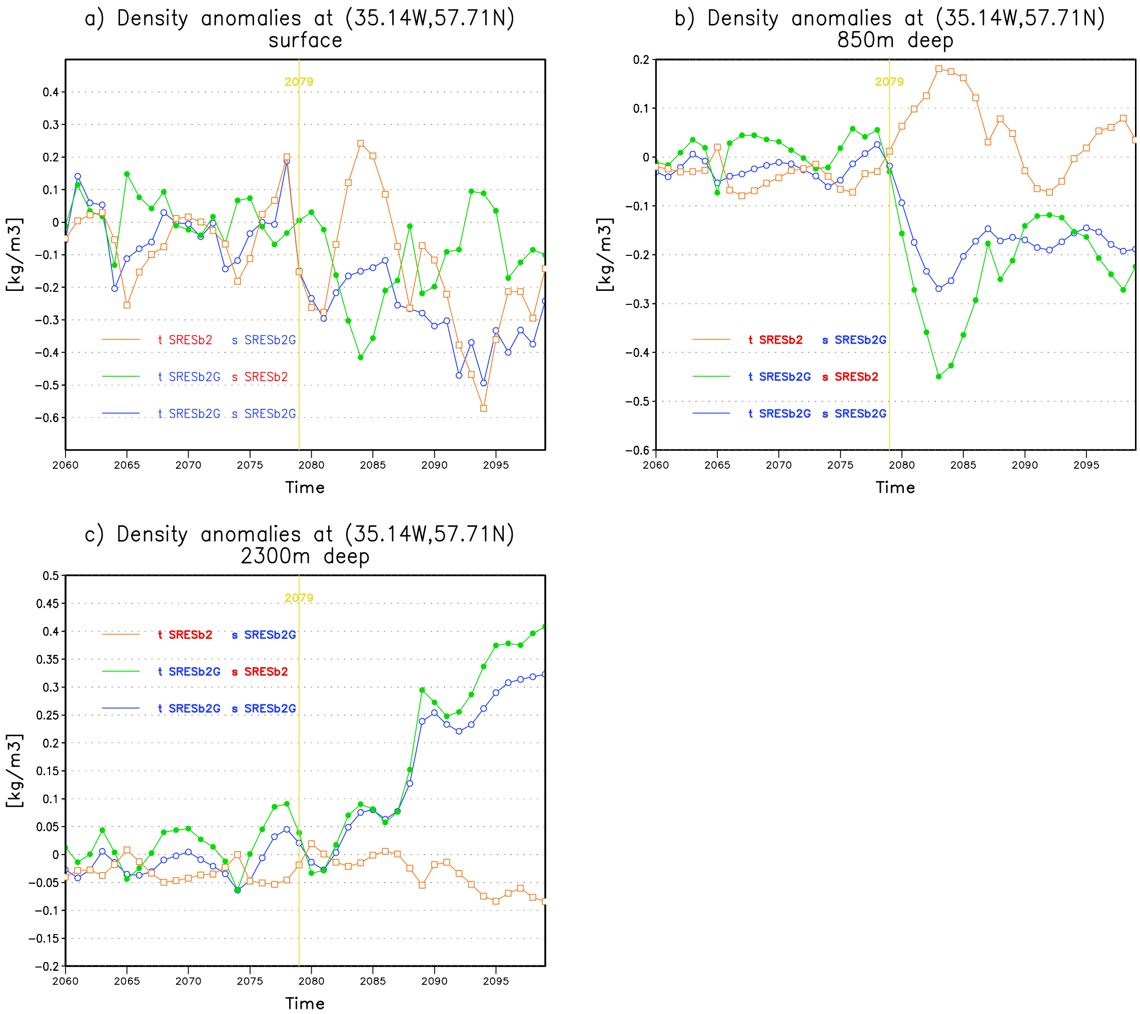

Figure 4.30: Time evolution of the surface density anomalies at (35.14°W, 57.71°N) (kg/m^3). The blue curve is the difference between the SRESb2G and SRESb2 simulations. A new density has then been computed using the SRESb2 salinity and the SRESb2G temperature to quantify the influence of temperature changes. The green curve is the difference between this new density and the SRESb2 values. Conversely, the orange curve shows the impact of salinity changes when the SRESb2 temperature and the SRESb2G salinity are used

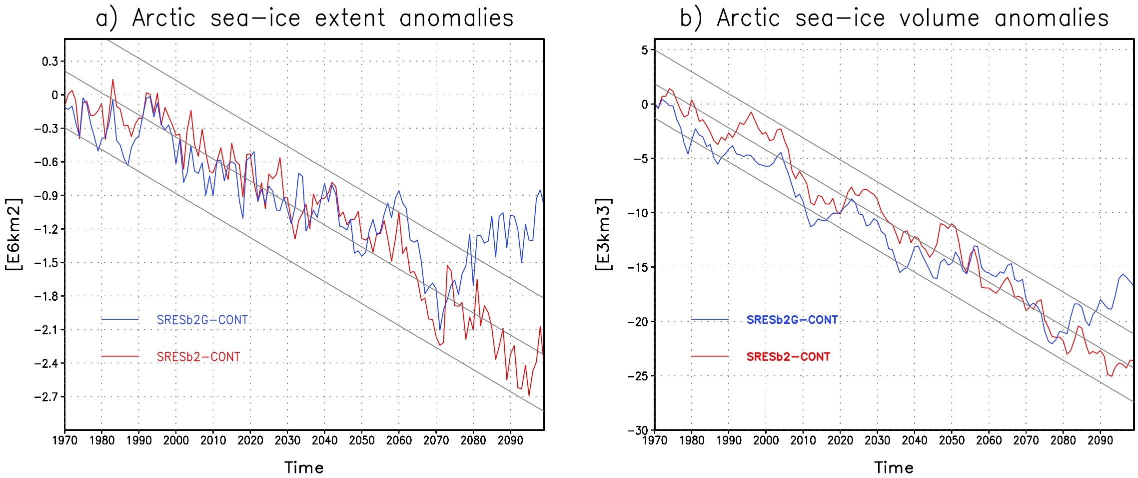

Figure 4.31: Time evolution of the annual mean Arctic sea-ice extent and volume in the scenario runs (SRESb2 and SRESb2G) compared to the CONT simulation.

At (36.42°W, 60.01°N), the surface freshening is strong and lengthy enough to win this competition. As a consequence, the vertical profiles are well mixed only down to 220 m. At (35.14°W, 57.71°N), the freshwater inflow at the surface is more sporadic, and it sometimes comes from the Baffin Bay and sometimes (later) from the Denmark Strait. Consequently, the density reduction at the surface is not as important as south-west of Iceland. Vertical mixing thus sometimes goes down to 850 m (depth of the density reduction that triggers mixing) and is sometimes constrained to the upper 400 m. This induces strong oscillations in the surface and mid-depth water characteristics. Nonetheless, deep convection never comes back, only "surface" mixing occurs. Furthermore, in both cases, AABW spreads northwards near the sea floor. The water temperature decreases at the base of the water column, which further inhibits deep convection.

4.2.3 Impacts on climate

The climate response to the collapse of the North Atlantic thermohaline circulation is mainly local until the end of the simulation. This is not surprising. Deep convection disappears around year 2087, i.e., 10 years before the end of the simulation. This is long enough to modify the component of the climate system with the shortest time-scales, namely the atmosphere, but the other components would need a greater delay to significantly react to this change. Nonetheless, the atmosphere is not the only component that undergoes rapid modifications. As the NADW convection areas are close to the sea-ice margin, the sea-ice pack is very sensitive to any modification of the oceanic convection.

The time evolution of the annual mean Arctic sea-ice extent and volume (figure 4.31) exhibit significant changes between the three simulations (CONT, SRESb2, and SRESb2G). The sea-ice pack is progressively reduced by additional melting in both scenario runs (see section 4.1.4), but the response is altered by the enhanced Greenland freshwater discharge.

- First, the sea ice of the SRESb2G integration regains regions that were previously

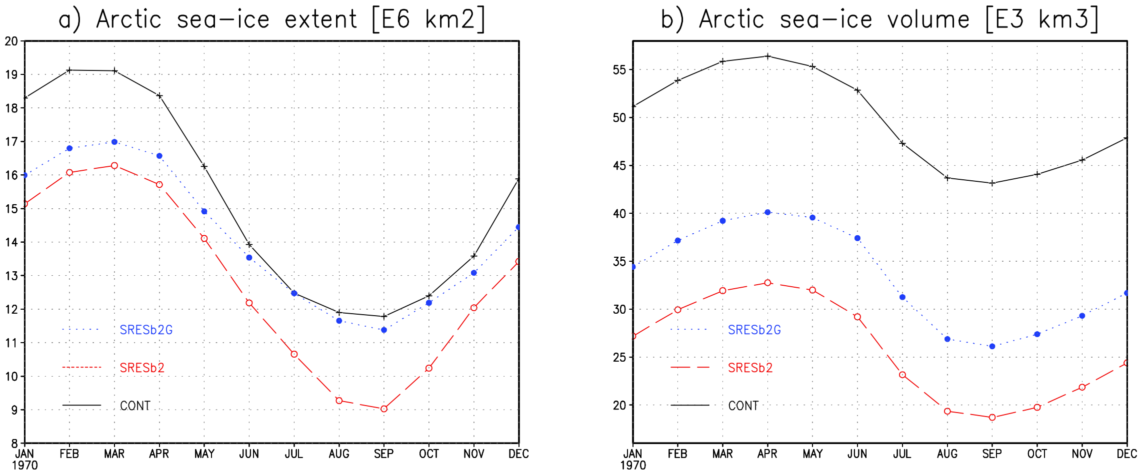

Figure 4.32: Seasonal cycles of Arctic sea-ice extent on the left and Arctic sea-ice volume on the right. The results of the three simulations (CONT, SRESb2, and SRESb2G) have been averaged from 2095 to 2099.

lost. This increase of the sea-ice extent is significant from 2081 in the SRESb2G simulation compared to the SRESb2 experiment.

- Sea-ice volume in SRESb2G needs some more time to go out of the confidence interval around the SRESb2 results (the signal becomes significant in 2086).

- Focusing on the last 5 years (2095-2099), the seasonal cycles of sea-ice extent and sea-ice volume are shown in figure 4.32. The sea-ice volume is enhanced in the SRESb2G simulation by about $7.5 \times 10^3\,\mathrm{km}^3$ throughout the year, but it is still strongly reduced compared to the CONT simulation. On the other hand, the sea-ice extent increase is more obvious in summer: the increase remains below $1 \times 10^6\,\mathrm{km}^2$ from November to March, but reaches $2.4 \times 10^6\,\mathrm{km}^2$ in August and September. Consequently, the winter extent forecasted by the SRESb2G experiment is closer to the SRESb2 simulation, whereas the summer extent comes back to the present-day values (CONT run).

To get more precise information, the geographical thickness distribution is displayed in figure 4.33 for both climate change experiments. The small increase in the winter extent, observed on the seasonal cycle when the simulation takes into account the impact of the Greenland runoff and calving, results from partial cancellation of the reduction of the sea-ice pack in the Pacific Ocean and the expansion in the Atlantic Ocean. In summer, the sea-ice margin is similar to the one simulated under present-day conditions (see chapter 3). Sea ice has disappeared in the Baffin Bay and drawn back northwards in the GIN Seas around 2080 in both SRESb2 and SRESb2G simulations, but since then, it spreads back southwards in both regions if the Greenland freshwater changes are taken into account (SRESb2G). Nonetheless, the impact of the greenhouse gases during the beginning of the simulation has already strongly melted sea ice, so thinner sea ice is found in the Arctic basin at the end of the SRESb2G simulation compared to the CONT simulation. This thickness difference reaches 3 m in the Kara Sea, 2 m in the central Arctic. The thickest sea ice

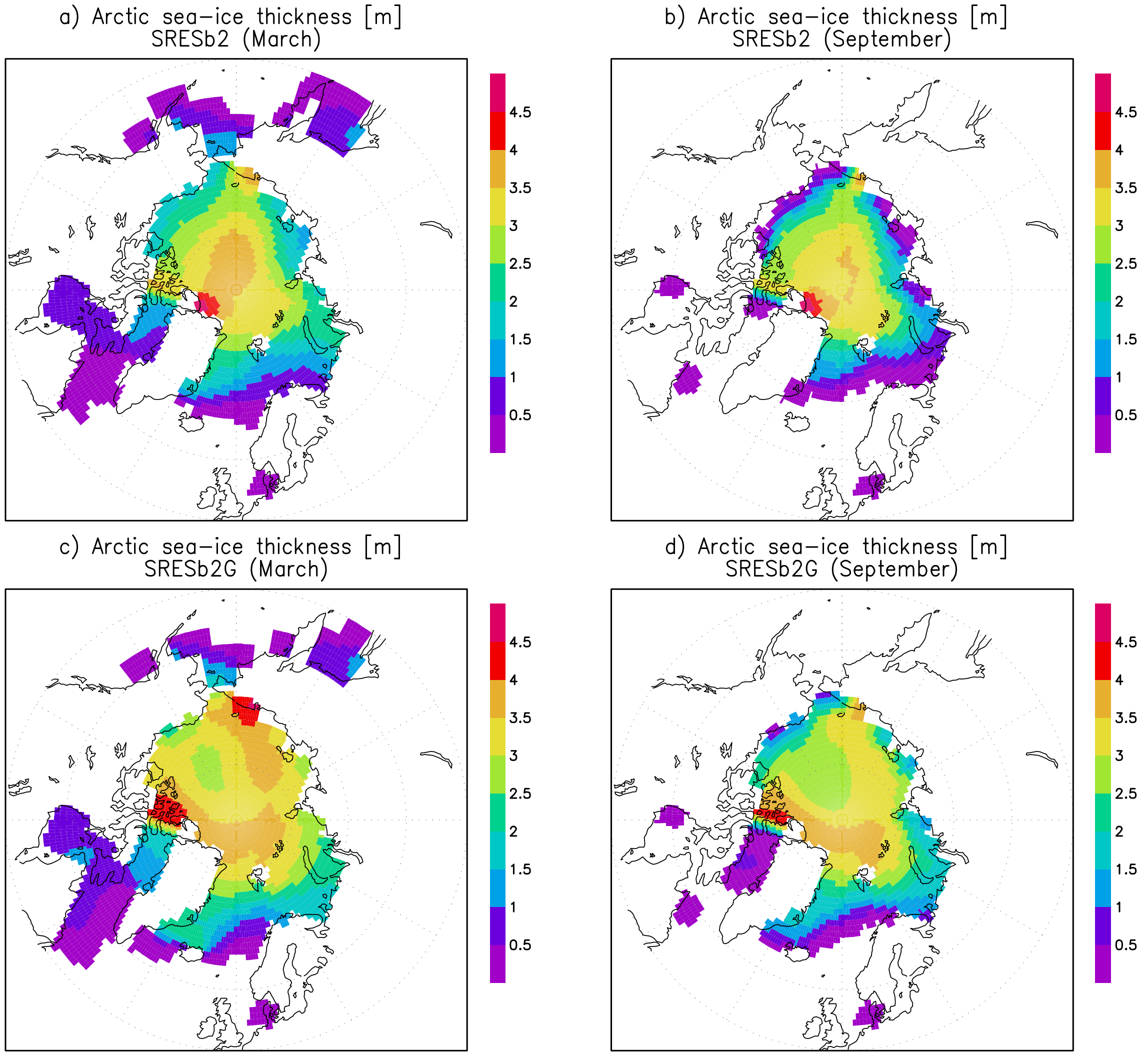

Figure 4.33: Arctic sea-ice thickness (m) in March and September in the SRESb2 (panels a, b) and SRESb2G simulations (panels c, d).

is simulated north of Greenland in the CONT simulation (see chapter 3) in reasonable agreement with observations. It remains at the same place in the SRESb2 simulation (see section 4.1.4) but decreases from 6.7m to 4.8m. On the other hand, the maximum thickness is shifted westwards to the Northwest Passage at the end of the SRESb2G experiment, but remains close to 4.3 m.

In the Southern Hemisphere, no clear modification of the sea-ice pack is observed between the SRESb2 and SRESb2G simulations.

The modifications of the Arctic sea ice, retreat in the North Pacific Ocean and extension in the North Atlantic Ocean, are connected to changes in the surface conditions. The ground and the surface air are significantly cooled over most of the Arctic ice pack (figure 4.34). A significant warming is also forecasted by LMD5-CLIO2 in the North Pacific Ocean. No other relevant signal on surface air temperature is simulated by LMD5-CLIO2 at any other place of the Earth between the SRESb2 and SRESb2G experiments. One can propound the following scenario to explain these temperature and sea-ice changes. The shutdown of the deep convection in the North Atlantic ocean induces a cooling of the surface layer. Consequently, sea ice invades this region and expands southwards in the Atlantic ocean. Sea ice furthers lower surface temperature and alters the air temperature. This local cooling in the North Atlantic modifies the atmospheric dynamics, which involves a warming in the North Pacific. Warmer atmospheric conditions then induce sea-ice melting in this region.

The winter response (figure 4.34a) is stronger getting to $+4°C$ for more than 10 points near Bering Strait and $-14°C$ north of Iceland (with a peak at $-23°C$). Over land, the signal is smaller except over the north and central Canada, which undergoes a $-6°C$ cooling in winter. The time evolution of the surface air temperature exhibits significant anomalies between the SRESb2 and SRESb2G simulations around 2082 when averaged between 60°N and 90°N (over other regions, no significant signal is obtained).

The SRESb2G anomalies (compared to the CONT simulation, figure 4.34e) can be contrasted with those of the SRESb2 experiment (figure 4.34d). While the SRESb2 run leads everywhere to a warming, the SRESb2G results indicate a strong cooling over the North Atlantic Ocean (especially near Greenland) and a smaller cooling over North America. Conversely, the temperature rise over the North Pacific ocean is enhanced in the SRESb2G simulation. Over Europe, the warming is slightly reduced in the SRESb2G experiment. Nevertheless, one should keep in mind that not all these features are significant as shown in figure 4.34c.

As expected, the surface air humidity anomalies (figure 4.35) are highly correlated to the surface air temperature changes. Indeed, Claudius-Clapeyron law links humidity at saturation and temperature: warmer air is able to keep more water vapour before saturation. Over the North Atlantic Ocean, less water vapour is simulated in the SRESb2G simulation as the surface is colder. On the contrary, warmer air over the North Pacific Ocean stores more humidity. These anomalies remain throughout the year. The modifications are not confined to the surface: the water content decrease near Iceland is obvious throughout the atmosphere and leads to significantly reduction of precipitable water and clouds. Over the North Pacific Ocean, precipitable water anomalies are also significant, but no cloud signal is detected.

This decrease of the atmospheric humidity near Iceland but also south of Greenland

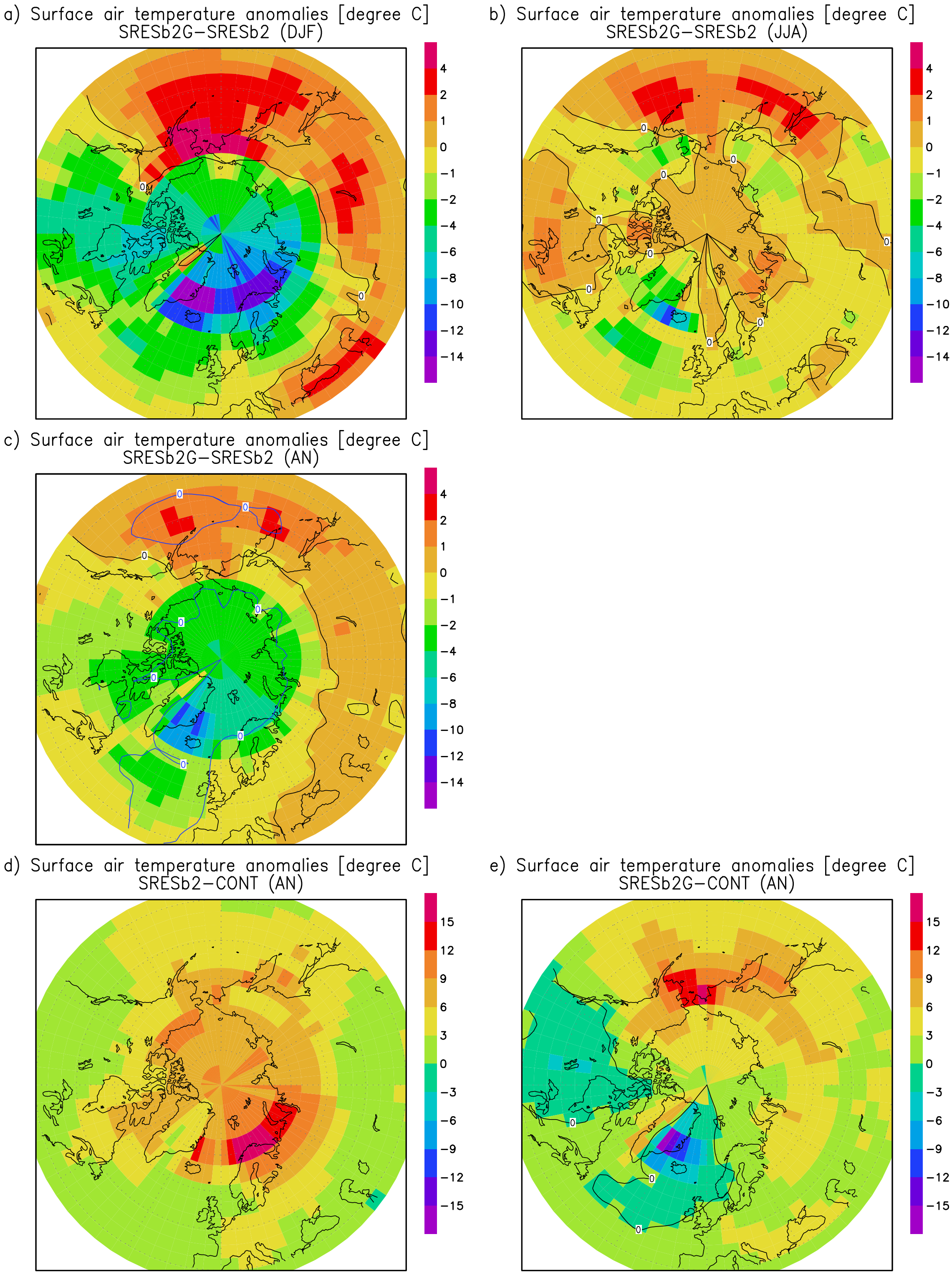

Figure 4.34: Surface air temperature anomalies (°C) between the two climate change experiments (SRESb2G-SRESb2) north of 40°N. Panels a and b respectively correspond to December-January-February and June-July-August. Panel c displays the annual mean. Zones where the signal is significant are surrounded by the blue curve. Panel d displays the anomalies in the SRESb2 simulations compared to the CONT simulation. Panel e shows the SRESb2G anomalies compared to the CONT simulation. All these results have been averaged over the last 5 years of the simulations (2095-2099).

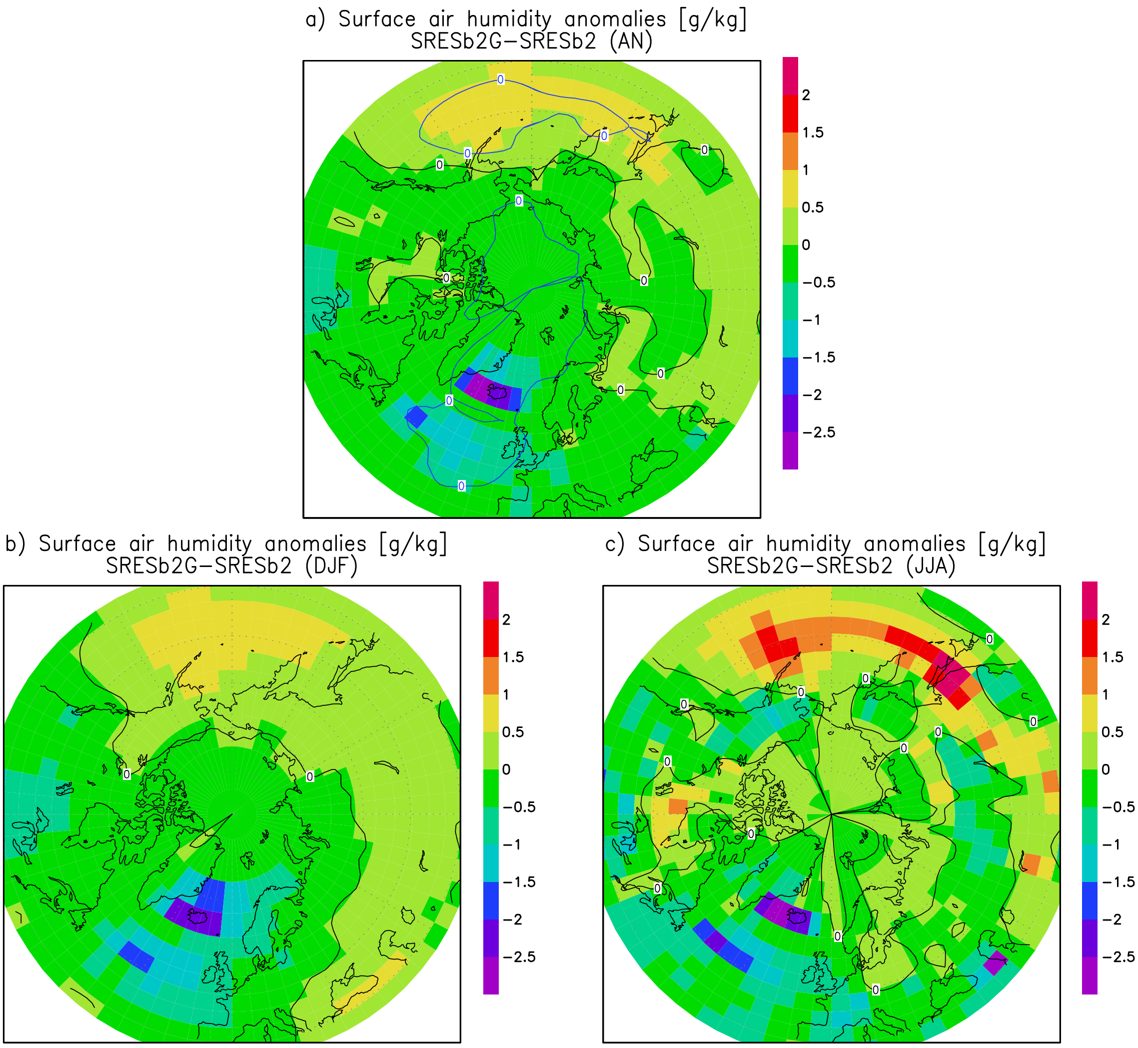

Figure 4.35: Surface air humidity anomalies (g/kg) between the two climate change experiments (SRESb2G-SRESb2) north of 40°N. Panel a displays the annual mean, and zones where the signal is significant are surrounded by the blue curve. Panels b and c correspond to December-January-February and June-July-August respectively. All these results have been averaged over the last 5 years of the simulations (2095-2099).

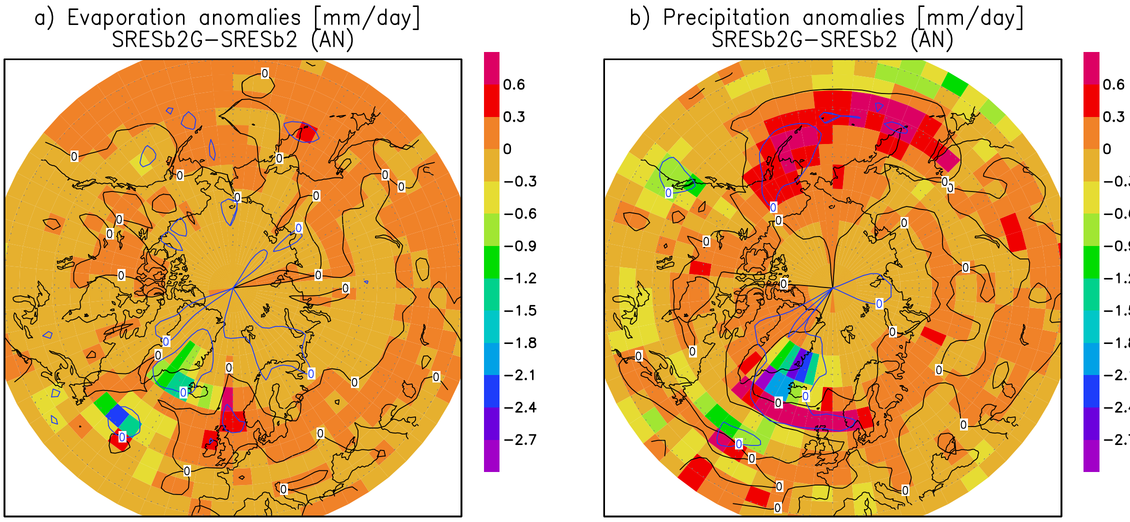

Figure 4.36: Annual mean evaporation anomalies (mm/day) and precipitation anomalies (mm/day) between the two climate change experiments (SRESb2G-SRESb2) north of 40°N are displayed respectively on panel a and b. The zones where the signal is significant are surrounded by the blue curve. All these results have been averaged over the last 5 years of the simulations (2095-2099).

and off Newfound Land is related to lower evaporation rate (figure 4.36). Near Iceland, extension of sea ice in winter insulates the atmosphere from the free ocean surface and therefore inhibits evaporation. South of Greenland, southward shift and weakening of North Atlantic Drift bring less warm tropical water off Newfound Land. Consequently, the westward atmospheric winds transporting dry and cold continental air from America towards the Atlantic Ocean overflows colder oceanic surfaces, reducing evaporation. Both phenomena mainly occur in winter, so the summer signal is much smaller than the winter one.

Precipitation is significantly reduced near Iceland (northward and westward of the island) and enhanced along a latitude band south of Iceland towards north of United Kingdom (figure 4.36). This pattern is related to modifications of the winter atmospheric circulation. The Icelandic Low is not as deep in the SRESb2G simulation and extends more eastwards. Consequently, surface winds bring humidity more zonally towards the United Kingdom (figure 4.37) where precipitation increases, and less towards Greenland and to the north where precipitation decreases. Over the North Pacific Ocean, the Aleutian Low is less pronounced in the SRESb2G than in the SRESb2 experiment and its eastward extension is further reduced. The high pressure zone centered near 35°N expands more northwards. Consequently, the westerlies blowing between these two pressure centers slightly shift northwards leading to positive precipitation anomalies over South Alaska and negative anomalies around the Vancouver area.

As all significant modifications of the hydrological cycle are located over the ocean, no clear change of the soil moisture is simulated by LMD5-CLIO2 in a response to the runoff and calving of the Greenland ice sheet.

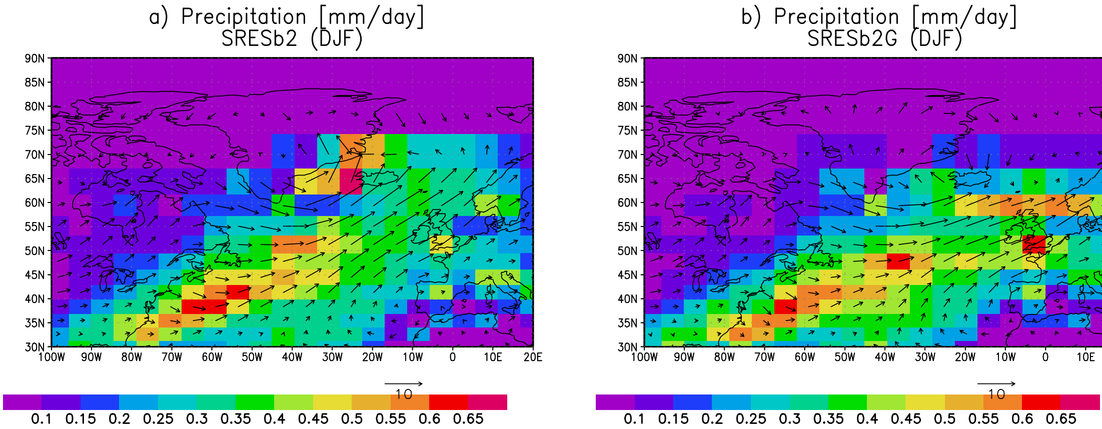

Figure 4.37: Winter precipitation (mm/day) simulated during the last 5 years (2094-2099) of the SRESb2 (panel a) and SRESb2G (panel b) experiments. Surface winds are superimposed.

Southwards, expansion of sea ice in the North Atlantic Ocean leads to the expected modifications of the surface heat fluxes. First, as sea ice insulates the oceanic surface from the atmosphere, the turbulent fluxes (sensible and latent heat fluxes) are reduced. Secondly, the surface does not absorb as much shortwave radiation because more solar radiation is reflected over sea ice than over free ocean (according to their albedo). Thirdly, the sea-ice surface temperature is lower than the free ocean temperature. Consequently, the longwave radiation emitted upwards by the surface is reduced (according to Stefan-Boltzmann's law). The atmospheric water content is cut down over most of this zone (see above). The overlying atmosphere is thus less efficient to trap radiation and less radiation comes back to the surface. These opposite influences lead to a reduction of the net upward longwave heat flux at the surface in the SRESb2G simulation.

4.3 Conclusion

The SRESb2 experiment analysis brings information about the future climate evolution as projected by LMD5-CLIO2. The surface air temperature rise is almost linear over the 21st century. It leads to a 2.4°C warming in 2100 compared to the CONT simulation. This value is in the middle range of those predicted by other AOGCMs using the same IPCC scenario. In the atmosphere, a maximum reaching 9°C in winter is simulated over the Northern Hemisphere high latitudes. A second maximum (about 5°C) is predicted in the high tropical troposphere as in most increasing greenhouse-gas simulations. The warming is also obvious in the ocean but it is mainly constrained to the surface mixed layer. Associated to this temperature increase, the hydrological cycle is amplified as a warmer atmosphere contains more humidity. Precipitation is stronger in the ITCZ and the summer Asian Monsoon is enhanced. The deep convection is more intense and brings more water vapour into the tropical atmosphere. Nevertheless, as the enhanced water condensation in the high tropical troposphere releases more latent heat (leading to the second warming maximum), the relative humidity is reduced at the top of the upward branch of the Hadley cells and in the downward branches. Consequently, evaporation increases over the subtropical oceans. Whereas clear signals are forecasted for the thermal and hydrological variables, no significant modification occurs in the atmospheric dynamics, except perhaps a reduction of the Southern Hemisphere westerlies. This weakening of the wind stress implies a decrease of the ACC intensity. Most significant changes in the oceanic dynamics deal with the thermohaline circulation, which is forced by modifications of the atmospheric heat and freshwater fluxes. The deep convection around Antarctica is less intense. Less cold and fresh surface water is thus brought to great depth. Furthermore, the additional heat available at the surface owing to the enhanced greenhouse effect is distributed by deep convection over the whole water column. Subsequently, the AABW is warmer and saltier. The NADW formation is also reduced.

Most of these changes are consistent with those predicted by other AOGCMs in similar studies. LMD5-CLIO2 in the SRESb2 experiment corroborates most expected features of future climate change. More surprising results arise from the SRESb2G simulation. This is the first time to our knowledge that an AOGCM coupled to a Greenland ice-sheet model forecasts an abrupt reduction of the intensity of the North Atlantic thermohaline circulation by the end of the 21st century.

In the SRESb2G simulation, the Greenland ice-sheet freshwater flux increases. It leads to the collapse of the NADW formation at the end of this run (around 2087). The freshening of the surface water between Greenland and Iceland where deep convection takes place in the CONT and SRESb2 simulations is linked to the Greenland ice-sheet water discharge. Indeed, it comes out that Greenland contributes to about 50% of the long-term change in total freshwater flux simulated by LMD5-CLIO2 over the North Atlantic ocean. The abrupt weakening of the NADW formation influences the Earth climate. Most impacts remain local in this simulation as this event occurs at the end of the run. Sea ice regains regions that were previously lost (due to the warming induced by greenhouse gases) in the North Atlantic ocean. On the contrary, the sea-ice margin moves polewards in the Pacific basin. These modifications of the sea-ice distribution are associated to the surface air temperature changes. A significant warming occurs over the North Pacific ocean while a cooling takes place over the North Atlantic ocean. As atmospheric humidity is altered by temperature changes, the surface specific humidity increases in the North Pacific. The North Atlantic response also involves the vertically integrated precipitable water and cloudiness. Furthermore, the Iceland Low location is modified. It implies more zonal winds near 60°N over the North Atlantic ocean. This brings more precipitation over and north of England and less south of Iceland. The North Pacific westerlies are slightly shifted northwards decreasing precipitation over Vancouver and increasing it over south Alaska.

The coupling of LMD5-CLIO2 with GISM enables us to investigate the potential collapse of the NADW formation and its impact on the global climate. The results of this simulation is by any way a prediction of what will happen in the future. It is only a possibility which is of course model-dependent and the projection would be different in another run which slightly different initial conditions. Nevertheless, it is a good opportunity to study this kind of event and to show up this possible future.

Conclusion

The aim of this work was to investigate the climate response to future increases in greenhouse-gas and sulphate-aerosol concentrations. To achieve this end, a coupled atmosphere-ocean general circulation model (AOGCM) called LMD5-CLIO2 has been integrated from 1970 to 2100 using the IPCC SRES B2 scenario (the SRESb2 and SRESb2G experiments). Prior to such climate-change simulations, a control run (CONT) had to be performed under present-day conditions in order to assess the ability of the model to simulate a realistic climate. As many other non-flux corrected AOGCMs, LMD5-CLIO2 diverges from the observed climate. The first years of any coupled simulation are characterized by a drift. In an AOGCM where processes at the air-sea interface are allowed to reach their own equilibrium, systematic errors can amplify: the atmospheric shortcomings on the surface heat fluxes alter the simulation of the sea-surface temperature by the oceanic component, which in turn alters the surface heat fluxes forecasted by the atmospheric component. Feedbacks can amplify initial errors.

Before performing long simulations, sensitivity experiments have thus been performed to improve the simulated climate, and reduce the initial drift. LMD5-CLIO2 is made up of three components: an atmospheric model (LMD5), a sea-ice and oceanic model (CLIO2), and a coupler which orchestrates the exchanges. All three components have been adapted to improve the model results. For example, the atmospheric vertical resolution has been increased, atmospheric parameters have been tuned. The atmospheric radiative scheme has been updated. The direct effect of the sulphate aerosols has been included in the model though modification of the surface albedo. Furthermore, a new version of the oceanic model has been adopted with a better representation of the vertical mixing and a new topography with an open passage between North America and Greenland. New fields are also transfered from CLIO2 to LMD5: the sea-ice and ocean albedos and the sea-ice thickness.

Thanks to all these modifications, the CONT simulation leads to acceptable results. Comparing the LMD5-CLIO2 simulated climate to observations, some deficiencies appear. The Antarctic sea ice melts rapidly at the beginning of the simulation. This is a common feature to many non-flux corrected models. The Arctic sea-ice extent and volume are slightly overestimated. Nevertheless, the thickness pattern is almost realistic and the seasonal cycle amplitude is correctly reproduced by the model. The main features of the tropical atmospheric and oceanic circulations are present in the LMD5-CLIO2 results: Trade Winds, the ITCZ and the SPCZ in the atmosphere; the North and South Equatorial Currents, the Equatorial Countercurrent and the Equatorial Undercurrent in the ocean. Nevertheless, inaccuracies in their location leads to temperature and salinity anomalies in the oceanic upper mixed layer. For example, the northward shift of the Pacific ITCZ modifies the precipitation pattern and consequently alters sea surface salinity. Moreover, this shift gives more place for the Equatorial Countercurrent which extends too far westwards into the Warm Pool. Sea-surface temperature anomalies are generated which moderate the SPCZ and the associated convective rainfall. In another respect, the North Atlantic deep convection zones are shifted to the south-west of Iceland. The underestimation of the Gulf Stream and the North Atlantic Drift in LMD5-CLIO2 does not bring enough warm water into the GIN seas. Consequently, the Barents, Kara and GIN Seas are covered by sea ice in the CONT simulation. At the same time, deep convection shuts down in this region. Nevertheless, while reduced, the NADW (North Atlantic Deep Water) formation does not collapse, it moves to another region. Furthermore, most LMD5-CLIO2 results stand within the range of the inter-model deviation deduced from the non-flux corrected AOGCMs participating to the first phase of the Coupled Model Intercomparison Project (CMIP1; *Lambert and Boer* [2001]). This assertion applies at least for sea-level pressure, surface air temperature, the net surface heat flux, the global oceanic heat transport, and precipitation.

The analysis of the CONT simulation concludes to the ability of LMD5-CLIO2 to simulate a realistic climate under present-day conditions. The next step is the climate-change experiments. The SRES B2 scenario has been used by other modeling teams to force their own AOGCMs. Consequently, LMD5-CLIO2 results could be compared to them. It comes out that the projection of the 21st climate in the SRESb2 simulation stands in the middle of the other model estimates. Indeed, LMD5-CLIO2 projects a global mean surface air temperature increase of 2.4°C in 2100, while the range suggested in *Cubasch et al.* [2001] is 0.9°C to 3.4°C. Furthermore, the surface air warming is also linear with time. The continental surface warming exceeds the increase of the sea-surface temperature. Two local maxima of temperature anomalies are simulated, one in the Northern Hemisphere high latitudes near the surface, the other in the tropics near the tropopause. There seems to be consensus today in the scientific community about these features. Moreover, the SRESb2 results show a strong meridional asymmetry with a strong warming in the Northern Hemisphere high latitudes and almost no significant warming over the Southern Ocean. This point has also been noted by the IPCC (*Cubasch et al.* [2001]) as most AOGCM projections share this characteristic. In another respect, the hydrological cycle is amplified in a warmer climate. LMD5-CLIO2 is able to trap this behaviour. The SRESb2 simulation undergoes a more or less linear increase in global mean precipitation. The relative anomalies (compared to the CONT run) reaches 3.3 % at the end of the 21st century. This is again in the middle range of the values projected by other models. Deep convection in the tropics and especially in the ITCZ is enhanced leading to heavier precipitation and freshening of the underlying ocean (in its mixed layer). The downward branches of the Hadley cells are dryer (their relative humidity is lower in the SRESb2 experiment than in the CONT simulation). Consequently, evaporation over the subtropical oceans is enhanced. The spatial distribution of precipitation changes is more noisy than for temperature changes. This is a well known characteristic of precipitation fields. It is thus difficult to compare the LMD5-CLIO2 predictions to those obtained with other AOGCMs as the inter-model deviation is large. By contrast, modifications of the atmospheric and surface oceanic circulations are small. The main response of the LMD5-CLIO2 dynamics to the increasing levels of greenhouse gases and sulphate aerosols is the reduction of the NADW formation. Looking at the freshwater flux at the top of the ocean, it comes out that this flux increases in the SRESb2 simulation compared to the CONT simulation over the North Atlantic Ocean. This ocean also releases less heat into the atmosphere. Both effects contribute to the stabilization of the water column and to the reduction of the deep convection in this area. Finally, the sea-ice response is spectacular. Melting of Arctic sea ice leads to a net freshwater flux of 0.0056 Sv into the ocean. Both its thickness and its effective area change (-1.1 cm/y and -20.6×10^3 km^2/y in average). Near the sea-ice margin, the ice/albedo feedback plays a leading role in the reduction of the sea-ice concentration. Further north, water feedback dominates and implies a strong reduction of the sea-ice thickness (about 1.5 m near the North Pole). Whereas these two feedbacks occur in summer, it has been explained that the maximum temperature anomalies take place in winter.

The last stage in this work studies the sensitivity of the simulated climate change to the Greenland ice-sheet water discharge. Consequently, the SRESb2G experiment is performed with LMD5-CLIO2 coupled to GISM. To our knowledge, it is the first simulation performed with such a coupling between an AOGCM and a Greenland ice-sheet model. Furthermore, it highlights the potential impact of the Greenland ice sheet on the oceanic thermohaline circulation during the 21st century. Indeed, it suggests that, by the end of the 21st century, the enhanced freshwater discharge by the Greenland ice sheet into the North Atlantic Ocean can shut down the NADW formation. While the two climate-change simulations (SRESb2 and SRESb2G) lead to similar results until 2075, they diverge during the last 25 years. The North Atlantic branch of the thermohaline circulation collapses at the end of the SRESb2G run. It has been shown that the origin of this event can be found in the increase of freshwater flux from Greenland.

Nevertheless, caution must be exercised when drawing conclusions from these experiments. Firstly, the present-day climate is not perfectly reproduced by LMD5-CLIO2. In particular, the main sites of deep convection are located east of the southern tip of Greenland and not in the GIN Seas and Labrador Sea as observed. This has certainly an influence on the sensitivity of the model to changes in the freshwater flux from Greenland. Owing to the analysis of the CONT simulation, it seems that the solution has to be found in a better representation of the Gulf Stream and the North Atlantic Drift. This dynamic problem in the ocean is linked to deficiencies in the atmospheric wind stress associated to the westerlies in the Northern Hemisphere mid-latitudes. The only suggestion we can formulate is to increase the atmospheric model resolution at mid- and high latitudes. This could help the model to simulate more accurately the main dynamic features.

A second element implies caution. Only one experiment has been conducted with an interactive ice sheet component and one without this component. Recent studies performed with Earth system models of intermediate complexity (e.g. *Knutti and Stocker* [2002]; *Schaeffer et al.* [2002]) have shown that evolution of the thermohaline circulation close to a transition point is quite unpredictable. Therefore, a large number of experiments would be necessary to demonstrate that the difference of behaviour between the SRESb2 and SRESb2G simulations is robust and does not arise by chance. Due to time limitation, this has not been done during this thesis because LMD5-CLIO2, as any AOGCM, requires large amounts of CPU time. It would be easier to perform such ensemble experiments with intermediate complexity models like ECBILT-CLIO (, also developed at the Institut d'Astronomie et de Géophysique G. Lemaître at the UCL).

By the end of the SRESb2G simulation, the shutdown of the NADW formation implies modifications of the climate. Among them, temperature and precipitation decrease in the vicinity of the Greenland ice sheet. This could lead to a negative feedback. Increasing temperature and precipitation induced by the greenhouse-gas and sulphate-aerosol modifications enhance the Greenland ice-sheet runoff and calving into the North Atlantic Ocean. This freshwater discharge alters oceanic salinity and therefore the thermohaline circulation leading to the collapse of the NADW formation. Reduction of convection enables sea ice to spread southwards in the North Atlantic. Consequently, temperature and precipitation are reduced in the surrounding of Greenland. This closes the feedback loop. Should this occur in the SRESb2G simulation ? To provide a response to this issue, the experiment should be continued.

As explained above, it would be interesting to perform ensemble experiments with and without coupling between LMD5-CLIO2 and GISM. This would give a stronger basis prior to conclude on the potential impact of the Greenland ice sheet during the 21st century.

The same study could be held with an Antarctic ice-sheet model. The AABW (Antarctic Bottom Water) formation can be sensitive to changes in the freshwater flux from Antarctica. However, the current version of the model is unable to simulate realistic Antarctic sea ice. It seems thus rash to undertake such an investigation. The LMD5-CLIO2 results in this region should first be improved. A track is the inclusion of the Gent and McWilliam's scheme (*Gent and McWilliams* [1990]) and the isopycnal diffusion scheme (*Redi* [1982]) in the oceanic component. This has already been done in another version (*Mathieu* [1998]). *Goosse et al.* [2001] has shown in forced mode that this modification in the CLIO model leads to a reduction of the open-water deep convection. Furthermore, *de Montety* [2003] identifies processes which links the Antarctic sea-ice extent to deep convection. In her work, sensitivity experiments to parameters involved in those two parameterizations were performed. The AOGCM used in that context was LMDZ-CLIO. That AOGCM is made of the new generation LMD's model and of a new version of the CLIO model. We could expect that similar conclusions could be drawn with LMD5-CLIO. However, the expected warming over Antarctica for the 21st century would probably not be strong enough to significantly increase the freshwater flux from the ice sheet. Consequently longer simulations would be needed to investigate this impact of Antarctica on the future climate. Currently, such long runs are hardly achieved with the CPU-time consuming AOGCMs and intermediate complexity models could be a good alternative.

List of acronyms

AABW Antarctic Bottom Water

AAIW Antarctic Intermediate Water

ACC Antarctic Circumpolar Current

AFORC Atmospheric forced simulation performed with LMD5

AGCM Atmosphere General Circulation Model

AOGCM Atmosphere Ocean General Circulation Model

ARPEGE AGCM developed at Météo-France (Toulouse)

CLIO2 OGCM developed at the UCL

COADS Comprehensive Ocean-Atmosphere Data Set

CONT Control simulation performed with LMD5-CLIO2

CMIP Coupled Model Intercomparison Project

CSM1 AOGCM developed at the NCAR

CPU Central Processing Units

DIC Dissolved Inorganic Carbon

DJF December-January-February

DOC Dissolved Organic Carbon

ECMWF European Center for Medium Range Weather Forecasts, Reading, United Kingdom

ENSO El-Nino Southern Oscillation

ERBE Earth Radiation Budget Experiment

GIN Greenland-Iceland-Norway

GISM Greenland Ice-Sheet Model developed at the VUB

IPCC Intergovernmental Panel on Climate Change

IPSL Institut Pierre-Simon Laplace in Paris.

ISCCP International Satellite Cloud Climatology Project

ITCZ Inter-Tropical Convergence Zone

JJA June-July-August

LMD Laboratoire de Météorologie Dynamique in Paris.

LMD5 AGCM originating from the LMD and improved at the UCL.

LWC Liquid Water Content

NADW North Atlantic Deep Water

NASA National Aeronautics and Space Administration, USA

NCAR National Center for Atmospheric Research in Boulder, Colorado

NCEP National Centers for Environmental Prediction, USA

OFORC Forced oceanic simulation performed with CLIO2

OGCM Ocean General Circulation Model

OPAICE OGCM developed at the IPSL in Paris

PBL Planetary Boundary Layer

PRISM Program for Integrated Earth System Modelling

PVM Parallel Virtual Machine

SAT Surface air temperature

SECHIBA Vegetation and soil parameterization in LMD5

SPCZ South Pacific Convergence Zone

SRES Special Report on Emissions Scenarios, IPCC, Cambridge university press.

SRESb2 Climate change simulation performed with LMD5-CLIO2 using the IPCC SRES B2 scenario

SRESb2G Climate change simulation performed with LMD5-CLIO2-GISM using the IPCC SRES B2 scenario

SSS Sea-surface salinity

SST Sea-surface temperature

TKE Turbulence kinetic energy

TOA Top of the atmosphere

UCL Université catholique de Louvain, Louvain-la-Neuve, Belgium

VUB Vrije Universiteit Brussel, Belgium

Bibliography

Arakawa, A., and V. Lamb, Computational design of the basic dynamical processes of the ucla general circulation model, in *Methods in Computational Physics*, edited by J. Chang, vol. 17, pp. 173–265, Academic Press, New York, 1977.

Baede, A., E. Ahlonsou, Y. Ding, and D. Schimel, The climate system: an overview, in *Climate change 2001, The Scientific Basis. Contribution of Working Group I to the Third Assessment Report of the Intergovernmental Panel on Climate Change*, edited by J. Houghton, Y. Ding, D. Griggs, M. Noguer, P. van der Lindern, S. Dai, K. Maskell, and C. Johnson, Cambridge university press, 2001.

Baretta-Bekker, H. G., E. K. Duursma, and B. R. Kuipers (Eds.), *Encyclopedia of Marine Sciences*, Springer, 1998.

Barkstrom, B., and G. Smith, The earth radiation budget experiment: Science and implementation, *Rev. Geophys.*, *24*, 379–390, 1986.

Barthelet, P., L. Terray, and S. Valcke, Transient co2 experiment using the arpege/opaice non flux corrected coupled model, *Geophys. Res. Lett.*, *25*, 2277–2280, 1998.

Bearman, G. (Ed.), *Ocean Circulation*, Pergamon press and The Open University, 1993.

Boer, G., N. McFarlane, R. Laprise, J. Henderson, and J.-P. Blanchet, The canadian climate centre spectral atmospheric general circulation model, *Atmos.-Ocean*, *22*, 397–429, 1984.

Boville, B., and P. Gent, The NCAR climate system model, version one, *J. Climate*, *11*, 1115–1130, 1998.

Boville, B., J. Kiehl, P. Rasch, and F. Bryan, Improvements to the NCAR CSM-1 for transient climate simulations, *J. Climate*, *14*, 164–179, 2001.

Brasseur, G., J. Orlando, and G. Tyndall, *Atmospheric Chemistry and Global Change*, Oxford University Press, 1999, 654pp.

Bryden, H., D. Roemmich, and J. Church, Ocean heat transport across 24°n in the pacific, *Deep Sea Res.*, *38*, 297–324, 1991.

Cai, W., and P. Baines, Interactions between thermohaline- and wind-driven circulations and their relevance to the dynamics of the antarctic circumpolar current, in a coarse-resolution global ocean general circulation model, *J. Geophys. Research*, *101*, 14,073–14,093, 1996.

Campin, J.-M., Modélisation tridimensionnelle de la circulation générale océanique lors du dernier maximum glaciaire, Ph.D. thesis, Faculté des Sciences, Université catholique de Louvain, Louvain-la-Neuve, Belgique, 1997, 342pp.

Campin, J.-M., and H. Goosse, Parameterization of density-driven downsloping flow for a coarse-resolution ocean model in z-coordinate, *Tellus*, *51A*, 412–430, 1999.

Candel, S., *Mécanique des fluides*, 2 ed., Dunod, 1996, 451p.

Chalita, S., and H. LeTreut, The albedo of temperate and boreal forest and the northern hemisphere climate: a sensitivity using the LMD GCM, *Clim. Dyn.*, *10*, 231–240, 1994.

Charlson, R., and J. Heintzenberg (Eds.), *Aerosol Forcing of Climate*, J. Wiley & sons, 1995, 416pp.

Chuang, C., J. Penner, K. Taylor, A. Grossman, and J. Walton, An assessment of the radiative effects of anthropogenic sulfate, *J. Geophys. Res.*, *102*, 3761–3778, 1997.

Church, J., J. Gregory, P. Huybrechts, M. Kuhn, K. Lambeck, M. Nhuan, D. Qin, and P. Woodworth, Changes in sea level, in *Climate change 2001, The Scientific Basis. Contribution of Working Group I to the Third Assessment Report of the Intergovernmental Panel on Climate Change*, edited by J. Houghton, Y. Ding, D. Griggs, M. Noguer, P. van der Lindern, S. Dai, K. Maskell, and C. Johnson, Cambridge university press, 2001.

Codron, F., and R. Sadourny, Saturation limiters for water vapour advection schemes: impact on orographic precipitation, *Tellus*, *54A*, 338–349, 2002.

Comiso, J., D. Cavalieri, C. Parkinson, and P. Gloersen, Passive microwave algorithms for sea-ice concentration: A comparison of two techniques., *Remote Sens. Environ.*, *60*, 357–384, 1997.

Cubasch, U., G. Meehl, G. Boer, R. Stouffer, M. Dix, A. Noda, C. Senior, S. Raper, and K. Yap, Projections of future climate change, in *Climate change 2001, The Scientific Basis. Contribution of Working Group I to the Third Assessment Report of the Intergovernmental Panel on Climate Change*, edited by J. Houghton, Y. Ding, D. Griggs, M. Noguer, P. van der Lindern, S. Dai, K. Maskell, and C. Johnson, Cambridge university press, 2001.

Cushman-Roisin, B., *Introduction to geophysical fluid dynamics*, Prentice Hall, 1994, 320pp.

da Silva, A. M., C. C. Young, and S. Levitus, *Atlas of surface marine data 1994*, National Oceanic Atmospheric Administration, 1994.

de Montety, A., LMDz-CLIO, un nouveau modèle du système couplé atmosphère-océan-glace de mer pour l'étude des climats polaires, Ph.D. thesis, Faculté des Sciences, Université catholique de Louvain, Louvain-la-Neuve, Belgique, 2003, 187pp.

Deardorff, J., The counter-gradient heat flux in the lower atmosphere and in the laboratory, *J. Atmos. Sci.*, *23*, 503–506, 1966.

Deleersnijder, E., J.-P. van Ypersele, and J.-M. Campin, An orthogonal, curvilinear coordinate system for a world ocean model, *Ocean Modelling*, *100*, 7–10, 1993.

Dickens, G., The blast in the past, *Nature*, *401*, 752–755, 1999.

Dorman, J., and P. Sellers, A global climatology of albedo, roughness length and stomatal resistance for atmospheric general circulation models as represented by the simple biosphere model (sib), *J. Appl. Meteor.*, *28*, 833–855, 1989.

Ducoudré, N., K. Laval, and A. Perrier, SECHIBA, a new set of parameterizations of the hydrologic exchanges at the land/atmosphere interface within the LMD atmospheric general circulation model, *J. Climate*, *6*, 248–273, 1993.

Eckart, C., Properties of water. part ii. the equation of state of water and sea water at low temperatures and pressures, *Am. J. Sci.*, *256*, 225–240, 1958.

Ferraro, R., T. Sato, G. Brasseur, C. DeLuca, and E. Guilyardi, Modeling the earth system, in *International Geoscience and Remote sensign symposium*, 2003.

Fichefet, T., and M. Morales Maqueda, Sensitivity of a global sea ice model to the treatment of ice thermodynamics and dynamics, *J. Geophys. Res.*, *102 (C6)*, 12,609–12,646, 1997.

Fichefet, T., and C. Tricot, Influence of the starting date of model integration on projections of greenhouse-gas-induced climatic-change, *Geophys. Res. Lett.*, *19*, 1771–1774, 1992.

Fichefet, T., B. Tartinville, and H. Goosse, Sensitivity of the antarctic sea ice to the thermal conductivity of snow, *Geophys. Res. Lett.*, *27(3)*, 401–404, 2000.

Fichefet, T., H. Goosse, and M. Morales Maqueda, A hindcast simulation of the arctic and antarctic sea-ice variability, 1955-2001, *Polar Reseach*, *22(1)*, 91–98, 2003a.

Fichefet, T., C. Poncin, H. Goosse, P. Huybrechts, I. Janssens, and H. LeTreut, Implications of changes in freshwater flux from the greenland ice sheet for the climate of the 21st century, *Geophys. Res. Lett.*, 2003b, in press.

Flato, G., and G. Boer, Warming asymmetry in climate change simulations, *Geophys. Res. Lett.*, *28*, 195–198, 2001.

Folland, C., et al., Observed climate variability and change, in *Climate change 2001, The Scientific Basis. Contribution of Working Group I to the Third Assessment Report of the Intergovernmental Panel on Climate Change*, edited by J. Houghton, Y. Ding, D. Griggs, M. Noguer, P. van der Lindern, S. Dai, K. Maskell, and C. Johnson, Cambridge university press, 2001.

Fouquart, Y., and B. Bonnel, Computation of solar heating of the Earth's atmosphere: a new parameterization, *Beitr. Phys. Atmos.*, *53*, 35–62, 1980.

Ganachaud, A., and C. Wunsch, Improved estimates of global ocean circulation, heat transport and mixing from hydrographic data, *Nature*, *408*, 453–457, 2000.

Gent, P., and J. McWilliams, Isopycnal mixing in ocean general circulation models, *J. of Phys. Oceanogr.*, *20*, 150–155, 1990.

Gibson, J., P. Kallberg, S. Uppala, A. Hernandez, A. Nomura, and E. Serrano, ECMWF Re-Analysis Project Report No1, ERA description, *Tech. rep.*, ECMWF, Reading, UK, 1997.

Gill, A., *Atmosphere-Ocean Dynamics*, vol. 30 of *International geophysics series*, Academic Press, 1982, 662p.

Gloersen, P., W. Campbell, D. Cavalieri, J. Comiso, C. Parkinson, and H. Zwally, *Arctic and Antarctic Sea Ice, 1978-1987: Satellite passive-microwave observations and analysis*, NASA, 1992, 289 p.

Goosse, H., Modelling the large-scale behavious of the coupled ocean-sea–ice system, Ph.D. thesis, Faculté des Sciences, Université catholique de Louvain, Louvain-la-Neuve, Belgique, 1998, 213pp.

Goosse, H., J.-M. Campin, T. Fichefet, and E. Deleersnijder, Sensitivity of a global ice-ocean model to the Bering Strait throughflow, *Clim. Dyn.*, *13*, 349–358, 1997.

Goosse, H., E. Deleersnijder, T. Fichefet, and M. H. England, Sensitivity of a global coupled ocean-sea ice model to thte parameterization of vertical mixing, *J. Geophys. Res.*, *104*, 13,681–13,695, 1999.

Goosse, H., J. Campin, and B. Tartinville, The sources of antarctic bottom water in a global ice-ocean model, *Ocean Modelling*, *3*, 51–66, 2001.

Gordon, C., C. Cooper, C. Senior, H. Banks, J. Gregory, T. Johns, J. Mitchell, and R. Wood, The simulations of SST, sea ice extents and ocean heat transports in a version fo the hadley centre coupled model without flux adjustments, *Clim. Dyn.*, *16*, 147–168, 2000.

Grenfell, T., and D. Perovich, Spectral albedos of sea ice and incident solar irradiance in the southern beaufort sea, *J. Geophys. Res.*, *89(C3)*, 3573–3580, 1985.

Grenier, H., Grid connexion and related sub-grid scale motions in a global climate model, 1995, progress Report 1995/8.

Grenier, H., Les interactions air-mer dans le systeme climatique: une étude à l'aide d'un modèle couplé tridimensionnel océan-atmosphère-glace marine, Ph.D. thesis, Faculté des Sciences, Université catholique de Louvain, Louvain-la-Neuve, Belgique, 1997, 269pp.

Hall, M., and H. Bryden, Direct estimates and mechanisms of ocean heat transport, *Deep Sea Res.*, *29*, 339–359, 1982.

Harrison, E., P. Minnis, B. Barkstrom, V. Ramanathan, R. Cess, and G. Gibson, Seasonal variations of cloud radiative forcing derived from the earth's radiation budget experiment, *JGR*, *95*, 18,687–18,703, 1990.

Hartmann, D., *Global physical climatology*, International geophysics series, Academic press, 1994, 411p.

Hellerman, S., and M. Rosenstein, Normal monthly wind stress over the world ocean with error estimates, *J. Phys. Oceanogr.*, *13*, 1093–1104, 1983.

Henderson-Sellers, A., and K. McGuffie, *A climate modelling primer*, John Wiley and sons, 1987, 217p.

Heymsfield, A., and L. Donner, A scheme for parameterizing ice-cloud water content in general circulation models, *J. Atmos. Sci.*, *47*, 1865–1877, 1990.

Hibler, W., A dynamic thermodynamic sea ice model, *J. Phys. Oceanogr.*, *9*, 815–846, 1979.

Holfort, J., and G. Siedler, The meridional oceanic transports of heat and nutrients in the south atlantic, *J. Phys. Oceanogr.*, *31*, 5–29, 2001.

Holton, J., *An introduction to dynamic meteorology*, vol. 48 of *International Geophysics Series*, Academic Press, 1992, 511pp.

Houghton, J., L. M. Filho, B. Callander, N. Harris, A. Kattenberg, and K. Maskell (Eds.), *Climate change 1995, The Science of Climate Change*, Intergovernmental Panel on Climate Change, Cambridge university press, 1996.

Houghton, J., Y. Ding, D. Griggs, M. Noguer, P. van der Lindern, S. Dai, K. Maskell, and C. Johnson, *Climate change 2001, The Scientific Basis. Contribution of Working Group I to the Third Assessment Report of the Intergovernmental Panel on Climate Change*, Cambridge university press, 2001.

Houze, R., *Cloud dynamics*, vol. 53 of *International Geophysics Series*, Academic Press, 1993, 573pp.

Huybrechts, P., and J. de Wolde, The dynamic response of the greenland and antarctic ice sheets to multiple-century climatic warming, *J. Climate*, *12*, 2169–2188, 1999.

Huybrechts, P., A. Letréguilly, and N. Reeh, The greenland ice sheet and greenhouse warming, *Palaeogeogr., Palaeoclim., Palaeoecol. (Global and Planetary Change Section)*, *89*, 399–412, 1991.

Huybrechts, P., I. Janssens, C. Poncin, and T. Fichefet, The response of the greenland ice sheet to climate changes in the 21st century by interactive coupling of an AOGCM with a thermomechanical ice sheet model, *Ann. Glacial.*, *35*, 2002.

Jaeger, L., Monthly and areal patterns of mean global precipitation, in *Variations in the GlobalWater Budget*, edited by A. Street-Perrot, M. Beran, and R. Ratcliffe, pp. 129–140, D. Reidel Publishing Company, 1983.

Janssens, I., and P. Huybrechts, The treatment of meltwater retention in mass balance parameterizations of the greenland ice sheet, *Ann. Glaciol.*, *31*, 133–140, 2000.

Kantha, L., and C. Clayson, An improved mixed layer model for geophysical applications, *J. Geophys. Res.*, *99*, 25,235–25,266, 1994.

Killworth, P., Deep convection in the world ocean, *Rev. Geophys. and Space Phys.*, *21*, 1–26, 1983.

Kistler, R., et al., The ncep-ncar 50-year reanalysis: Monthly means cd-rom and documentation, *Bul. Amer. Meteor. Soc.*, *82*, 247–267, 2001.

Knutti, R., and T. Stocker, Limited predictability of the future thermohaline circulation close to an instability threshold, *J. Climate*, *15*, 179–186, 2002.

Kuo, H., On formation and intensification of tropical cyclones through latent heat release by cumulus convection, *J. Atmos. Sci.*, *22*, 40–63, 1965.

Kvenvolden, K., Gas hydrates–geological perspective and global change, *Rev. Geophys.*, *31*, 173–187, 1993.

Lambert, S., and G. Boer, CMIP1 evaluation and intercomparison of coupled climate models, *Climate Dynamics*, *17*, 83–106, 2001.

Lavin, A., H. Bryden, and G. Parrilla, Meridional transport and heat flux variations in the subtropical north atlantic, *The Global Atmos. Ocean System*, *6*, 269–293, 1998.

LeClainche, Y., Modélisation du ruissellement dans un modèle couplé océan-atmosphère, Ph.D. thesis, LSCE, France, 1996, dEA report.

Legates, D., and C. Willmott, Mean seasonal and spatial variability in gauge-corrected, global precipitation, *Intern. J. Climatology*, *10*, 111–127, 1990.

LeTreut, H., and Z.-X. Li, Sensitivity of an atmospheric general circulation model to prescribed SST changes: feedback effects associated with the simulation of cloud optical properties, *Clim. Dyn.*, *5*, 175–187, 1991.

Levitus, S., Climatological atlas of the world ocean, *NOAA Prof. Pap. 13*, U. S. Gov. Print. Office, 1982, 173pp.

Li, Z., Description algorithmique d'un ensemble de paramétrisation physique - phylmd, *Tech. rep.*, Laboratoire de Météorologie Dynamique du CNRS, 1998.

Liu, T., W. Tang, and F. Wentz, Precipitable water and surface humidity over global oceans from speciall sensor microwave imager and european center for medium range weather forecasts, *J. Geophys. Res.*, *97*, 2251–2264, 1992.

Louis, J., A parametric model of vertical eddy fluxes in the atmosphere, *Bound. Layer Meteo.*, *17*, 187–202, 1979.

MacDonald, A., and C. Wunsch, Oceanic estimates of global ocean heat transport, *US WOCE Rep*, pp. 28–30, 1996.

Manabe, S., and R. Strickler, Thermal equilibrium of the atmosphere with a convective adjustment, *J. Atmos. Sci.*, *21*, 361–385, 1964.

Mathieu, P.-P., Parametrization of mesoscale turbulence in the world ocean, Ph.D. thesis, Faculté des Sciences, Université catholique de Louvain, Louvain-la-Neuve, Belgique, 1998, 248pp.

Matthews, E., Global vegetation and land use: new high-resolution databases for climate studies, *J. Climate Appl. Meteor.*, *22*, 474–487, 1983.

Matthews, E., Vegetation, land use, and seasonal albedo datasets: documentation of archived tape, *Tech. rep.*, National Aeronautics and Space Administration, Washington, D.C., 1984, tech. Memo. 86107.

McAvaney, B., et al., Model evaluation, in *Climate change 2001, The Scientific Basis. Contribution of Working Group I to the Third Assessment Report of the Intergovernmental Panel on Climate Change*, edited by J. Houghton, Y. Ding, D. Griggs, M. Noguer, P. van der Lindern, S. Dai, K. Maskell, and C. Johnson, Cambridge university press, 2001.

Meehl, G., G. Boer, C. Covey, M. Latif, and R. Stouffer, The Coupled Model Intercomparison Project (CMIP), *Bull. Am. Met. Soc.*, *81*, 313–318, 2000.

Mellor, G., and T. Yamada, Development of a turbulence closure model for geophysical fluid problems, *Rev. Geophys. Space Phys.*, *20*, 851–875, 1982.

Mesinger, F., and A. Arakawa, Numerical methods used in atmospheric models, Vol. 1, GARP Series 17, WMO-ICSU, 1976.

Milliman, J., and R. Meade, World-wide delivery of rever sediment to the oceans, *J. of Geology*, *91*, 1–21, 1983.

Mitchell, J., R. Davis, W. Ingram, and C. Senior, On surface temperature, greenhouse gases, and aerosol: Models and observations, *J. Climate*, *8*, 2364–2386, 1995.

Mitchell, J., D. Karoly, G. Hegerl, F. Zwiers, M. Allen, and J. Marengo, Detection of climate change and attribution of causes, in *Climate change 2001, The Scientific Basis. Contribution of Working Group I to the Third Assessment Report of the Intergovernmental Panel on Climate Change*, edited by J. Houghton, Y. Ding, D. Griggs, M. Noguer, P. van der Lindern, S. Dai, K. Maskell, and C. Johnson, Cambridge university press, 2001.

Morales Maqueda, M., Un modelo acoplado del hielo de mar y del oceano superficial para estudios climaticos, Ph.D. thesis, Univesidad Camplutense Madrid, Madrid, Spain, 1995, 426pp.

Morcrette, J.-J., Impact of changes to the radiation transfer parameterizations plus cloud optical properties in the ECMWF model, *Mon. Wea. Rev.*, *118*, 847–873, 1990.

Morcrette, J.-J., Radiation and cloud radiative properties in the ECMWF operational weather forecast model, *J. Geophys. Res.*, *96*, 9121–9132, 1991.

Nakićenovic, N., et al., *Special Report on Emissions Scenarios*, Cambridge university press, 2000, a Special Report of Working Group III of the Intergovernmental Panel on Climate Change.

Nowlin, W., and J. Klinck, The physics of the Antartic Circumpolar Current, *Rev. Geophys.*, *24*, 469–491, 1986.

Pacanowski, R., and S. Philander, Parameterization of vertical mixing in numerical models of tropical ocean, *J. Phys. Oceanogr.*, *11*, 1443–1451, 1981.

Paulson, C., and J. Simpson, Irradiance measurements in the upper ocean, *J. Phys. Oceanogr.*, *7*, 952–956, 1977.

Payne, R., Albedo of the sea surface, *J. Atmos. Sci.*, *29*, 959–970, 1972.

Penner, J., C. Chuang, and K. Grant, Climate forcing by carbonaceous and sulfate aerosols, *Climate Dynamics*, *14*, 839–851, 1998.

Penner, J., et al., Aerosols, their direct and indirect effects, in *Climate change 2001, The Scientific Basis. Contribution of Working Group I to the Third Assessment Report of the Intergovernmental Panel on Climate Change*, edited by J. Houghton, Y. Ding, D. Griggs, M. Noguer, P. van der Lindern, S. Dai, K. Maskell, and C. Johnson, Cambridge university press, 2001.

Pond, S., and G. Pickard, *Introductory Dynamical Oceanography*, Pergamon Press, 1983, 329p.

Prather, M., et al., Atmospheric chemistry and greenhouse gases, in *Climate change 2001, The Scientific Basis. Contribution of Working Group I to the Third Assessment Report of the Intergovernmental Panel on Climate Change*, edited by J. Houghton, Y. Ding, D. Griggs, M. Noguer, P. van der Lindern, S. Dai, K. Maskell, and C. Johnson, Cambridge university press, 2001.

Prentice, I., et al., The carbon cycle and atmospheric carbon dioxide, in *Climate change 2001, The Scientific Basis. Contribution of Working Group I to the Third Assessment Report of the Intergovernmental Panel on Climate Change*, edited by J. Houghton, Y. Ding, D. Griggs, M. Noguer, P. van der Lindern, S. Dai, K. Maskell, and C. Johnson, Cambridge university press, 2001.

Rahmstorf, S., Bifurcations of the atlantic thermohaline circulation in response to changes in the hydorlogical cycle, *Nature*, *378*, 145–149, 1995.

Ramade, F., *Eléments d'écologie, écologie fondamentale*, McGrawHill, 1987, 403pp.

Redi, M., Oceanic isopycnal mixing by coordinate rotation, *J. Phys. Oceanogr.*, *12*, 1154–1158, 1982.

Reeh, N., Parameterisation of melt rate and surface temperature on the greenland ice sheet, *Polarforschung*, *59*, 113–128, 1991.

Rintoul, S., South atlantic inter-basin exchange, *J. Geophys. Res.*, *96*, 2675–2692, 1991.

Roemmich, D., J. Gibson, G. Cornuelle, and R. Weller, The mean and time-varying meridional transport of heat at the tropical subtropical boundary of the north pacific ocean, *J. Geophys. Res.*, *106*, 8957–8970, 2001.

Rossow, W., and R. Schiffer, ISCCP cloud data products, *Bull. Amer. Meteo. Soc.*, *72*, 2–20, 1991.

Sadourny, R., The dynamics of finite difference models of the shallow water equations, *J. Atmos. Sci.*, *32*, 680–689, 1975a.

Sadourny, R., Compressible model flows on the sphere, *J. Atmos. Sci.*, *32*, 2103–2110, 1975b.

Sadourny, R., Conservation laws, turbulence, and numerical modelling of large-scale flow, in *1979 ECMWF Seminar*, pp. 167–195, European Centre for Medium-Range Weather Forecasts, Reading, 1980.

Sadourny, R., and K. Laval, January and July performance of the LMD general circulation model, in *New Perspectives in Climate Modeling*, edited by A. Berger and C. Nicolis, pp. 173–197, 1984.

Sato, O., and T. Rossby, Seasonal and low-frequency variability of the meridional heat flux at 36°n in the north atlantic, *J. Phys. Oceanogr.*, *30*, 606–621, 2000.

Saugier, B., *Végétation et atmosphère*, Dominos, Flammarion, 1996, 127pp.

Schaeffer, M., F. Selten, H. Goosse, and J. Opsteegh, Intrincis limits to predictability of abrupt regional climate change in ipcc sres scenarios, *Geophys. Res. Lett.*, *29(16)*, 10.1029/2002GL015,254, 2002.

Schmitz, W., On the interbasin-scale thermohaline circulation, *Res. Geophys.*, *33*, 151–173, 1995.

Semtner, A., A model for the thermodynamic growth of sea ice in numerical investigations of climate, *J. Phys. Oceanogr.*, *6*, 379–389, 1976.

Shine, K., and A. Handerson-Sellers, The sensitivity of a thermodynamic sea ice model tot changes in surface albedo parameterization, *J. Geophys. Res.*, *90(D1)*, 2243–2250, 1985.

Smagorinsky, J., S. Manabe, and J. Holloway, Results from a nine-level general circulation model of the atmosphere, *Mon. Wea. Rev.*, *93*, 727–768, 1965.

Stocker, T., Past and future reorganizations in the climate system, *Quat. Sci. Rev.*, *19*, 301–319, 2000.

Stommel, H., Thermohaline convection with two stable regimes of flow, *Tellus*, *13*, 225–230, 1961.

Sundqvist, H., Prediction of stratiform clouds: results of a 5-day forecast with a global model, *Tellus*, *33*, 242–253, 1981.

Trenberth, K., and J. Caron, Estimates of meridional atmopshere and ocean heat transports, *J. Climate*, *14*, 3433–3443, 2001.

Trenberth, K., and A. Salomon, The global heat balance: heat transports in the atmosphere and ocean, *Climate Dynamics*, *10*, 107–134, 1994.

Trenberth, K., J. Olson, and W. Large, A global ocean wind stress climatology based on ecmwf analyses, *National Center for Atmos. Res.*, *NCAR/TN-338+STR, Boulder, Colorado*, 93 pp, 1989.

UNESCO, Mean monthly and extreme discharges (1976-1979), in *Discharge of selected rivers of the world*, vol. 3, UNESCO press, 1985.

Warren, S., C. Hahn, J. London, R. Chervin, and R. Jenne, Global distribution of total cloud cover and cloud type amounts over the ocean, *NCAR Technical Notes NCAR/TN-317+STR and DOE Technical Report No. DOE/ER-0406*, U.S. Department of Energy, Carbon Dioxide Research Division, 1988.

Xie, P., and P. Arkin, Analyses of global monthly precipitation using gauge observations, satellite estimates and numerical model predictions, *J. Climate*, *9*, 840–858, 1996.